This is a repository copy of *Phase distribution, composition, and disorder in Y2(Hf,Sn)2O7 ceramics: insights from solid-state NMR spectroscopy and first-principles calculations*.

White Rose Research Online URL for this paper:
https://eprints.whiterose.ac.uk/165261/

Version: Accepted Version

Article:

Phase Distribution, Composition and Disorder in $Y_2(Hf,Sn)_2O_7$ Ceramics: Insights from Solid-State NMR Spectroscopy and First-Principles Calculations

Robert F. Moran,[1] Arantxa Fernandes,[1] Daniel M. Dawson,[1] Scott Sneddon,[1]
Amy S. Gandy,[2] Nik Reeves-McLaren,[2] Karl R. Whittle[2,3]
and Sharon E. Ashbrook,[1]*

[1]*School of Chemistry, EaStCHEM and Centre of Magnetic Resonance, University of St Andrews,*
St Andrews KY16 9ST, United Kingdom

[2]*Department of Materials Science and Engineering, University of Sheffield,*
Mappin Street, Sheffield S1 3JD, UK

[3]*School of Engineering, University of Liverpool, Brownlow Hill, Liverpool, L69 3GH, UK*

*Author to whom correspondence should be addressed.

Email: *sema@st-andrews.ac.uk*

Abstract

A NMR crystallographic approach, combining ^{89}Y, ^{119}Sn and ^{17}O NMR spectroscopy with X-ray diffraction and first-principles calculations has been used investigate the number and type of phases present, and the local structure and disorder in $Y_2Hf_{2-x}Sn_xO_7$ ceramics. Although a phase change is predicted with increasing Hf content, NMR spectra clearly show the presence of a significant two-phase region, with a Sn-rich pyrochlore and relatively Hf-rich defect fluorite phase co-existing for much of the compositional series. A single-phase pyrochlore is found only for the Sn end member, and a single defect fluorite phase only for x = 0 to 0.2. A solid-solution limit of ~10% is seen for the substitution of Hf into $Y_2Sn_2O_7$, although no evidence is seen for any cation ordering or antisite disorder in this phase. In the defect fluorite phase there is preferential ordering of oxygen vacancies around Sn, which is only ever seen in a six-coordinate environment. The remaining vacancies are more likely to be associated with Hf than with Y, although this distinction is less apparent at higher Sn concentrations. To acquire ^{17}O NMR spectra samples were post-synthetically exchanged with ^{17}O$_2$(g), although high temperatures (> 900 °C) were required to ensure uniform enrichment of different chemical species. Although these ^{17}O NMR spectra confirm the formation of mixed-metal materials and the presence of two phases, more quantitative analysis is hindered by the overlap of signals from pyrochlore and defect fluorite phases. In all cases, DFT calculations play a vital role in the interpretation and assignment of the NMR spectra, and in understanding the local structure and disorder in these complex multi-phase materials.

Introduction

Ceramic $A_2B_2O_7$ oxides find application in a wide range of areas, including in the electronics industry, as photocatalysts, as energy materials and in the encapsulation of radioactive waste.[1-5] Such oxides adopt different structures depending on the relative sizes of the A and B cations, with the pyrochlore structure (space group $Fd–3m$) favoured when r_A/r_B is between 1.46 and 1.78.[6-8] As shown in Figure 1a, this can be considered as a superstructure of fluorite (AO_2), with the ordered removal of 1/8 of the oxygen atoms, leading to an eight-coordinate A site and a six-coordinate B site. The crystal chemical flexibility of the pyrochlore structure enables a diverse range of substitutions, thereby altering the physical and chemical properties of the material and, ultimately, its end applications. However, such substitutions can change r_A/r_B significantly, and when this ratio falls below 1.46 a defect fluorite phase is generally adopted (space group $Fm–3m$) as shown in Figure 1b,[6-8] with a random distribution of both cations and anions/vacancies, leading to an average cation coordination number of 7.

The physical and chemical properties of ceramics are intimately linked to their local structure and disorder. However, the possibility of a change in structure type with composition raises a number of questions, including the nature of the atomic disorder present, whether a true solid solution is formed, or if two (or more) phases are present simultaneously and, in the latter case, if there are any compositional differences between them. In general, the structural characterization of disordered materials can be difficult, with approaches based on Bragg diffraction providing a picture only of the average structure. The presence of multiple phases (and any compositional differences between them) poses additional challenges for routine measurements.

Nuclear magnetic resonance (NMR) spectroscopy is a complementary tool for the study of complex and disordered systems, with an inherent sensitivity to the local atomic-scale environment without the need for any long-range order.[9-11] In particular, the chemical shift interaction has been shown to be sensitive to the number, type and position of the

surrounding atoms. In recent years, the combined application of experimental NMR spectroscopy, diffraction and first-principles calculations to predict NMR parameters – an approach sometimes referred to as NMR crystallography – has been used to aid spectral understanding and assignment and, ultimately, the extraction of detailed structural information.[12-14] This combined approach has been employed to investigate cation disorder in $Y_2(Sn,Ti)_2O_7$ pyrochlore solid solutions,[15-18] and to study $Y_2(Zr,Sn)_2O_7$[19] and $La_2(Sn,Ti)_2O_7$[20] materials, where phase transitions (from pyrochlore to a defect fluorite and a layered perovskite-like phase, respectively) are predicted.

In this work, we combine multinuclear NMR spectroscopy and first-principles calculations to investigate the phase evolution, local structure and disorder in $Y_2(Hf,Sn)_2O_7$ ceramics, where a phase change is predicted, from pyrochlore to defect fluorite, with increasing Hf content. Although NMR spectroscopy is relatively straightforward to implement for ^{89}Y (100% natural abundance) and ^{119}Sn (8.6%), both of which have spin quantum number I = 1/2,[9] such measurements provide only an indirect measure of the cation distribution, *i.e.*, via changes in chemical shift resulting from variation in the next nearest neighbour (NNN) environment. Furthermore, ^{119}Sn will not necessarily be present in every phase, making it challenging to determine accurately the proportion (and composition) of the phases present in multi-component systems. Although Hf NMR spectroscopy is possible (^{177}Hf, 18.6%, I = 7/2 and ^{179}Hf, 13.6%, I = 9/2), the very large quadrupole moments for both isotopes results in extremely broad spectral lines (often broadened over many MHz), limiting resolution and the structural information available.[9,21-22] In contrast, ^{17}O (I = 5/2) has a much smaller quadrupole moment (enabling resolution enhancement techniques such as magic-angle spinning (MAS) to be implemented more easily).[9,21-22] Oxygen is present in equal amounts in $A_2B_2O_7$ phases, irrespective of Sn/Hf content, and is directly coordinated to the cations of interest (thereby providing a more direct measure of their distribution). However, routine study of ^{17}O is typically prevented by its low natural abundance (0.037%), requiring isotopic enrichment to achieve good sensitivity and to acquire spectra on a reasonable timescale.[23] Recent work investigating the enrichment of pyrochlore and defect fluorite phases showed that while isotopic enrichment was possible

4

via post-synthetic exchange with $^{17}O_2$ (g), considerable care had to be taken regarding the choice of enrichment temperatures and times to mitigate preferential enrichment of chemically different O species.[24]

Here, we show that by combining information from ^{89}Y, ^{119}Sn and ^{17}O NMR spectroscopy, with spectral interpretation in each case supported by first-principles calculations, it is possible to gain insight into the type, proportion and composition of the phase(s) present in $Y_2(Hf,Sn)_2O_7$ ceramics as the Hf content changes, and to gain information about the level and type of disorder observed. The results demonstrate the potential of this combined approach for the structural characterisation of disordered ceramics; a vital first step in understanding the structure-property relationships in these materials, and the ultimate future design of new materials.

Methods

Synthesis and basic characterisation

Ceramic oxides with composition $Y_2Hf_{2-x}Sn_xO_7$ (x = 0.0 to 2.0) were synthesised using a conventional mixed-metal oxide process. Stoichiometric quantities of commercially available Y_2O_3 (Sigma Aldrich, 99%), SnO_2 (Sigma Aldrich, 99.9%) and HfO_2 (Sigma Aldrich, 99%) were heated to 850 °C for 10 h followed by ball milling, using ZrO_2 balls and cyclohexane as the milling medium. After drying, the resultant powders were pressed into pellets using a uniaxial press. Samples were then heated to 1500 °C in air at a rate of 5 °C min^{-1} for 168 h followed by cooling in the furnace at ~20 °C min^{-1}. Samples were characterised by powder X-ray diffraction (pXRD) using a Panalytical Empyrean Diffractometer, operating at 45 mA, and 40 kV, with an X'celerator linear detector. Scans were collected over the 2θ range of 5-100°, using an integrated step size of 0.0167°, and equivalent counting time of 75.8 s per step (total experimental time of 2 hours). Powder patterns are shown in the Supporting Information.

17O enrichment

Following the procedure used in Ref. 24, all $Y_2Hf_{2-x}Sn_xO_7$ (x = 0.0 to 2.0) materials were enriched in ^{17}O post synthesis, by condensing ~0.03 L of 70% $^{17}O_2(g)$ (Cortecnet) into a pre-evacuated quartz vial containing ~0.2 g of oxide, before heating in a tube furnace at 900 °C for 12-24 h. A ramp rate of 5 °C min^{-1} was used for heating and cooling. As described in Ref. 24, the level of enrichment in $Y_2Hf_2O_7$ (enriched at 900 °C for 24 h) was measured using Secondary Ion Mass Spectrometry (SIMS) as ~7.5%. After enrichment, no significant changes were seen in pXRD patterns and ^{89}Y MAS NMR spectra.

Solid-state NMR spectroscopy

^{89}Y NMR spectra were acquired using a Bruker Avance III 600 MHz NMR spectrometer, equipped with a widebore 14.1 T magnet, at a Larmor frequency of 29.41 MHz. Powdered samples were packed into 4 mm Si_3N_4 rotors to prevent any ^{89}Y background signal, and rotated at 14 kHz, using a 4 mm HX low-γ probe. Spectra were acquired using a radiofrequency field strength of ~22 kHz (π/2 ≈ 11.3 μs) and a recycle interval of 10 s. Although T_1 is relatively long for all ^{89}Y resonances, there is little difference in the relative relaxation rates, and spectral intensities accurately reflect the relative site populations even at shorter recycle intervals. MAS spectra were acquired using either a spin echo (to ensure accurate acquisition of the broad components) or using a Carr-Purcell-Meiboom-Gill (CPMG)[25-26] echo train to increase sensitivity. In the latter case, ~600 echoes were typically acquired, with a frequency-domain spikelet spacing of 167 Hz. Chemical shifts are given in ppm relative to the primary reference 1 M aqueous YCl_3, measured using a secondary reference compound, $Y_2Ti_2O_7$, at 65 ppm.

^{119}Sn NMR spectra were acquired using a Bruker Avance III 400 MHz spectrometer, equipped with a widebore 9.4 T magnet, at a Larmor frequency of 149.2 MHz. Powdered samples were packed into 4 mm ZrO_2 rotors and rotated at 14 kHz, using a 4 mm HX probe. Spectra were acquired using a spin echo, with a radiofrequency field strength of ~100 kHz (π/2 ≈ 2.5 μs) and a recycle interval of 30 s, and are the result of averaging between 224 and 2048 transients. Chemical shifts are given in ppm relative to the primary

reference $(CH_3)_4Sn$, measured using a secondary reference compound, SnO_2, at -604.3 ppm.

[89]Y and [119]Sn CSA parameters were measured using two-dimensional CSA-amplified PASS NMR experiments were carried out using the pulse sequence of Orr *et al.*[27-28] Fitting of the sideband patterns in the indirect dimension was carried out using SIMPSON,[29] as described in the Supporting Information. Full experimental details for these measurements are also given in the Supporting Information.

^{17}O NMR spectra were acquired using a Bruker Avance III 600 MHz spectrometer, equipped with a widebore 14.1 T magnet, at a Larmor frequency of 81.4 MHz. Powdered samples were packed into 3.2 mm thin-walled ZrO_2 rotors and rotated at 21 kHz, using a 3.2 mm HX probe. Spectra were acquired using a radiofrequency field strength of ~71 kHz, a pulse duration of 0.5 μs ($\pi/14$) and a recycle interval of 1 s, and are the result of averaging 8192 transients. Chemical shifts are given in ppm relative to distilled H_2O (l). The [17]O MQMAS spectrum of $Y_2Sn_{0.6}Hf_{1.4}O_7$ was acquired using a z-filtered pulse sequence[30] with ν_1 of ~71 kHz for excitation and conversion pulses and a CT-selective (ν_1 of ~3 kHz) $\pi/2$ pulse. The spectrum is the result of acquiring 3384 transients for each of 24 t_1 increments of 71.4 μs. The spectrum is shown after shearing and is referenced to the δ_1 axis referenced according to the convention in Ref. 31.

Calculations

Calculations of total energies and NMR parameters were carried out using the CASTEP density functional theory (DFT) code (version 8.0,[32-33] employing the gauge-including projector augmented wave (GIPAW) approach[32] to reconstruct the all-electron wavefunction in the presence of a magnetic field. Calculations were performed using the GGA PBE functional[34] and core-valence interactions were described by ultrasoft pseudopotentials,[35] accounting for scalar relativistic effects using ZORA.[36] A planewave energy cutoff of 60 Ry (~816 eV) was used, and integrals over the first Brillouin zone were performed using a Monkhorst-Pack grid[37] with a k-point spacing of 0.04 2π Å^{-1}. All

calculations were converged as far as possible with respect to both k-point spacing and energy cutoff. In the geometry optimisation all atomic coordinates and unit cell parameters were allowed to vary, with an energy tolerance of 1×10^{-5} eV per atom and an electronic structure energy tolerance of 1×10^{-9} eV per atom used. See the Supporting Information for details on the generation of substituted pyrochlore and defect fluorite models.

Diagonalisation of the absolute shielding tensor, $\boldsymbol{\sigma}$, yields the three principal components, σ_{11}, σ_{22} and σ_{33}, from which the isotropic shielding can be determined by $\sigma_{iso} = (\sigma_{11} + \sigma_{22} + \sigma_{33})/3$. To facilitate comparison to experimental measurement, the corresponding chemical shift tensor, $\boldsymbol{\delta}$, the computed isotropic shift δ_{iso} and the corresponding principal components of the shift tensor, δ_{ii} (where $\delta_{11} \geq \delta_{22} \geq \delta_{33}$), can be determined. See Supporting Information for details of the procedures used in this work. The magnitude of the anisotropy is determined is defined by the span, $\Omega = \delta_{11} - \delta_{33}$, and the skew, $\kappa = 3 (\delta_{22} - \delta_{iso})/\Omega$, is a measure of the asymmetry of the tensor. Diagonalisation of the electric field gradient tensor, V, gives the principal components V_{XX}, V_{YY} and V_{ZZ}, where $|V_{ZZ}| \geq |V_{YY}| \geq |V_{XX}|$. From these the magnitude of the quadrupolar interaction, $C_Q = eQV_{ZZ}/h$, where Q is the nuclear quadrupole moment (for which a value of 25.58 mb was used for ^{17}O)[38] and the asymmetry parameter, $\eta_Q = (V_{XX} - V_{YY})/V_{ZZ}$ can be determined. The quadrupolar product, $P_Q = C_Q(1 + \eta_Q^2/3)^{1/2}$.

Results and Discussion

^{89}Y MAS NMR

Figure 2 shows ^{89}Y MAS NMR spectra of $Y_2Hf_{2-x}Sn_xO_7$, acquired using either a spin echo or a CPMG sequence. The substitution of Hf into $Y_2Sn_2O_7$ should result in a change from a pyrochlore to a defect fluorite structure which, by simple radius ratio considerations, should occur between Y_2HfSnO_7 and $Y_2Hf_{1.2}Sn_{0.8}O_7$.[6,7] For $Y_2Sn_2O_7$, a single peak is observed in the NMR spectrum at ~150 ppm, in good agreement with previous

literature,[15,39-40] confirming the presence of Y on the eight-coordinate A site of an ordered pyrochlore. The spectrum observed for the second end member, $Y_2Hf_2O_7$, is very different, with three broadened resonances at ~88, ~190 and ~285 ppm, the latter of which has very low intensity. The broadened lineshapes observed are consistent with the formation of a defect fluorite phase, with disorder on both cation and anion sub lattices. The spectrum is similar to that for $Y_2Zr_2O_7$,[19,41] and by analogy, it is expected that the peaks correspond to six-, seven- and eight-coordinate Y in order of decreasing chemical shift. This conclusion is supported by DFT calculations for 34 models of defect fluorite $Y_2Hf_2O_7$, generated as described in the Supporting Information. As shown in Figure 3a, a decrease in the Y coordination number results in a change in the average calculated ^{89}Y δ_{iso} of ~100 ppm per O. From spectral integration, the relative amounts of six-, seven- and eight-coordinate Y are 2%, 47% and 51%, respectively.

As Hf is substituted into $Y_2Sn_2O_7$ additional ^{89}Y resonances are observed at lower chemical shift. By analogy with previous work on $Y_2(Sn,Ti)_2O_7$ and $Y_2(Zr,Sn)_2O_7$,[15,18-19,40] it might be expected that these result from the substitution of increasing numbers of Hf on to the six NNN B sites that surround each Y. This conclusion is supported by DFT calculations, carried out for a series of pyrochlore models where the environment around one Y species is systematically modified to vary the number (and relative position) of Hf and Sn on the NNN B sites (see Supporting Information for more details). As shown in Figure 3b, DFT calculations predict a decrease in the calculated ^{89}Y δ_{iso} of ~30 ppm per Hf substituted. Little difference is seen for different spatial arrangements of the same number of Sn/Hf species on the six B sites. Consequently, the signals at ~148, ~125 and ~103 ppm can be assigned to Y with Sn6, Sn5Hf and Sn4Hf2 NNN, respectively.

The DFT calculations carried out also predict a significant change in ^{89}Y Ω with a change in the number of Sn or Hf NNN, as shown in the Supporting Information. This parameter was shown to be a sensitive probe of local structure in previous work on $Y_2Ti_{2-x}Sn_xO_7$, where a strong correlation of Ω with the average Y-O_{8a} bond distance was observed.[17,18] For $Y_2(Hf,Sn)_2O_7$ pyrochlores, the calculations predict a change in ^{89}Y Ω of ~90 ppm per Hf

9

substituted onto the NNN B sites (see Figure S2.4). Owing to the difficulties associated with measuring CSA parameters experimentally using slow MAS experiments, particularly if there is more than one site present, CSA-amplified PASS experiments were employed[27,28] (see the Supporting Information). CSA parameters were measured for the sharp resonances present in the spectra of samples with x = 2.0 to 1.0. (It was not possible to extend these experiments to samples with higher Hf content owing to the increasing intensity of broader, overlapped resonances). The parameters extracted (along with one example of an experimental CSA-amplified PASS spectrum, analytical fits and contour plots of the rms error) are given in the Supporting Information. Although, in general, the calculated Ω appears overestimated when compared to experiment, the computed and experimental trends are in good agreement and so support the spectral assignment. (It should be noted that the low intensity of the peak attributed to Sn4Hf2 in all spectra significantly increases the experimental uncertainty of the measurement as the Hf content increases). Previous [89]Y CSA measurements on related pyrochlore materials applied a scaling factor to calculated values of Ω for comparison to experiment.[17] This approach has not been employed here owing to the small number of data available, and only the trends in the measurements have been considered.

The three resonances at ~148, ~125 and ~103 ppm appear in all [89]Y NMR spectra from x = 2.0 to x = 0.4, suggesting a pyrochlore-like phase is present over this entire compositional range. However, only three resonances are ever observed in any sample (*i.e.*, the fourth, fifth or sixth peaks predicted by the DFT calculations shown in the Supporting Information, resulting from an increasing number of Hf NNN, are not seen). Furthermore, the relative intensities of the three peaks (and their chemical shifts) are very similar in each spectrum in which they appear (see Table 1 and Supporting Information), indicating similar levels of Hf substitution in the pyrochlore phase, despite the increasing amount of Hf in the starting materials. This suggests that there is a relatively low solid solution limit for Hf in $Y_2Sn_2O_7$, and that the remaining Hf is being incorporated into a separate (*i.e.*, defect fluorite) phase.

Figure 2 shows that broad peaks found for the $Y_2Hf_2O_7$ defect fluorite phase are also clearly present in the ^{89}Y NMR spectra for samples with x = 0 to x = 1.2. With increasing levels of Sn in the starting synthesis there are changes in the relative intensities and width/shape of the peaks (see Supporting Information), confirming that Sn is substituting into the defect fluorite phase. Noticeably, there is also a loss of the signal attributed to six-coordinate Y. Analytical fitting of the ^{89}Y NMR spectra of the x = 1.4 to 1.8 materials show that a better fit is obtained when these broader resonances are also included (see Supporting Information for an example), as was observed for $Y_2(Zr,Sn)_2O_7$ ceramics,[19] suggesting a significant two-phase region is present in this system.

From a fitting of each of the ^{89}Y MAS NMR spectra, the relative intensities of the individual resonances can be determined. Assuming that the sharp resonances can be attributed solely to the pyrochlore phase, and the broader resonances to the defect fluorite phase (and assuming a formula of $Y_2X_2O_7$ in both cases), it is possible to determine the relative proportions of pyrochlore and defect fluorite phases present, as shown in Figure 4a. This suggests a significant amount of a defect fluorite phase is present even when the Hf content is relatively low (although it should be noted that the error on these values is greater, owing to the increased error in the fitting of the low intensity but much broader lines), and approximately equal amounts of the two phases are seen for x = 1.6. A single defect fluorite phase is observed only between x = 0.4 and 0.0. This picture is very different from that predicted by simple radius ratio rules, but is similar to the behavior seen in previous work on $Y_2(Zr,Sn)_2O_7$[19] albeit with a slightly wider two-phase region in the system studied here.

As the resonances observed for the pyrochlore phase can be attributed to Y with different numbers of Sn/Hf NNN, their relative intensities can, in principle, provide information on the composition (*i.e.*, the proportion of Sn and Hf) of this phase with a variation in x. Subsequently, knowing the overall proportions of Sn and Hf used in that starting mixture (and assuming there are no significant impurity phases and no starting materials remain – a reasonable assumption given the lack of evidence for these in the NMR spectra and

pXRD patterns), it is possible to determine the relative proportion of Sn and Hf (*i.e.*, the composition) of the defect fluorite phase. Figure 4b shows the relative proportions of Sn and Hf in the two phases as a function of the nominal composition, and reveals the solid solution limit of Hf in $Y_2Sn_2O_7$ is ~10%, *i.e.*, corresponding to a composition of $Y_2Hf_{0.2}Sn_{1.8}O_7$. There is no significant variation in the composition of the pyrochlore phase as the nominal composition (*i.e.*, that of the starting materials) varies while, in contrast, a much more significant change is seen for the defect fluorite phase. The much greater amount of Sn that can be incorporated into $Y_2Hf_2O_7$ explains the more significant changes in peak position discussed earlier (see also Supporting Information). Figure 4c plots the proportion of the total amount of Sn (and Hf) incorporated in the pyrochlore and defect fluorite phases as a function of the nominal (starting) composition. For example, when x = 1.8, just over 80% of the Hf present is incorporated into the defect fluorite phase, and ~20% is found in the pyrochlore phase.

^{119}Sn MAS NMR

Further information on the phases present, their compositions and the local environments of the species within them can be obtained using ^{119}Sn NMR spectroscopy. Figure 5 shows ^{119}Sn MAS NMR spectra of $Y_2Hf_{2-x}Sn_xO_7$, acquired using a spin echo sequence. The position and relative intensities of the peaks seen are given in Table 2 and in the Supporting Information. For $Y_2Sn_2O_7$, a single peak is observed in the NMR spectrum at –582.6 ppm, in good agreement with previous literature,[16,18,42] and characteristic of a six-coordinate Sn species. As Hf is substituted additional resonances are observed at lower shift, at ca. –588 ppm and –591 ppm (see also fitting in the Supporting Information). These resonances are relatively narrow, suggesting they result from an ordered phase and, based on chemical shift, also correspond to six-coordinate Sn. As shown in Figure 6a, DFT calculations confirm a decrease in ^{119}Sn δ_{iso} of ~8 ppm as one Hf is substituted onto the six NNN B sites that surround each Sn, suggesting these resonances result from Sn with Sn6, Sn5Hf and Sn4Hf2 NNN environments, respectively. However, Figure 6a shows that the predicted magnitude of the change decreases as the Hf content increases. This is different from the corresponding plot for ^{89}Y (in Figure 3b), but is more similar to the behavior seen for the

$Y_2(Sn,Ti)_2O_7$ pyrochlore solid solution (where the overlap of the signals predicted for different local environments was more significant),[16,18] and for $Y_2(Zr,Sn)_2O_7$ ceramics.[19] DFT calculations also predict only a small change in [119]Sn Ω with increasing Hf content (see Supporting Information). However, this parameter is challenging to measure accurately experimentally (as shown in the Supporting Information), owing to the low intensity of the spectral resonances at lower shift. Although Figure 6a suggests it might become more difficult to resolve individual signals for pyrochlores with higher Hf content on the basis of δ_{iso}, it should be noted that the relative intensities of the three resonances seen experimentally do not vary significantly with the nominal composition of the sample, supporting the general conclusion from the [89]Y NMR data that there is little change in the Hf content of the pyrochlore phases formed in different samples.

For the sample with the lowest Sn content (x = 0.2), a broad [119]Sn resonance is seen at −616 ppm, corresponding to Sn in the disordered defect fluorite phase. This signal shifts to higher δ with increasing Sn content (see Table 2). This resonance is clearly present for samples with x = 0.2 to 1.2, but analytical fits for samples with x = 1.4 to 1.8 are also improved when a broad component is included, as shown in the Supporting Information. This confirms the presence of a broad two-phase region in this system (from x = 1.8 to 0.4), as observed by [89]Y NMR. Unlike the analysis of the [89]Y NMR spectra, the intensities of the [119]Sn resonances cannot easily be used to provide information directly on the absolute proportion of the phases present as the Sn is not equally distributed between them. Furthermore, the greater overlap of the pyrochlore and defect fluorite peaks, and the low level of Sn present in some materials makes an accurate analysis of the relative intensities much more challenging than for [89]Y.

All of the resonances in the ^{119}Sn NMR spectra in Figure 5 have chemical shifts associated with six-coordinate Sn species, suggesting not only that Sn is confined to the B site in the pyrochlore phase, but that it also exclusively adopts six-fold coordination in the disordered defect fluorite phase, i.e., that the vacancies are preferentially associated with Sn over Y or Hf. This conclusion is supported by DFT calculations for modified $Y_2Sn_2O_7$

pyrochlore structures, where one or two 8a O atoms are moved to the vacant 8b sites surrounding each Sn. As shown in Figure 6b, an increase in coordination number results in a significant decrease in chemical shift (of ~200 ppm per coordinated O). No [119]Sn signal is observed at these values experimentally (as shown in the Supporting Information for x = 0.2), confirming only six-coordinate Sn is present in all defect fluorite phases.

^{17}O MAS NMR

Figure 7 shows ^{17}O MAS NMR spectra of $Y_2Hf_{2-x}Sn_xO_7$, enriched at 900 °C for 12 h. There are two crystallographically distinct O species in the pyrochlore structure; O1 (8a, coordinated by four A cations) and O2 (48f, coordinated by two A and two B cations). For some pyrochlores, the definition of O1 and O2 is reversed, but here we follow the crystallographic notation used in Ref. 43. Recent work has demonstrated that relative [17]O enrichment of these two sites in $Y_2Sn_2O_7$ was non quantitative at lower temperatures (*i.e.*, for exchange at temperatures below 700 °C), with preferential enrichment of O2.[24] Only at higher enrichment temperatures (or longer durations at lower temperatures) were consistent relative spectral intensities achieved. In contrast, uniform [17]O enrichment of the defect fluorite end member, $Y_2Hf_2O_7$, was achieved at much lower temperatures.[24] As many of the materials studied here are mixed phase, it is also necessary to consider the relative enrichment levels of the two phases under the conditions used. As shown in the Supporting Information (using a 1 : 1 physical mixture of $Y_2Sn_2O_7$ and $Y_2Hf_2O_7$) uniform relative enrichment of the pyrochlore and defect fluorite phases is achieved by enrichment at 900 °C for 12 h. However, as shown in previous work, the relative spectral intensities need to be corrected for differences in relaxation between the different sites and the contribution of the satellite transitions (STs) to the spectrum.[24]

The ^{17}O MAS NMR spectrum of $Y_2Sn_2O_7$ is in good agreement with that published previously,[24] with two signals observed. The signal corresponding to the O1 (OY4) species has a very small C_Q (reflecting its very symmetrical local environment), while that attributed to O2 (OY2Sn2) has a much larger C_Q (3.2 MHz). The relative intensities of the two signals (~1 : 1.82) reflects the 1 : 6 ratio expected once corrections for differences in

relaxation and the contribution of the STs have been applied, as described in Ref. 24. The ^{17}O MAS NMR spectrum of $Y_2Hf_2O_7$ is also in good agreement with that published previously,[24] and contains a complex composite spectral lineshape. In principle, the cation disorder present in the defect fluorite phase results in five different local environments (OY4, OY3Hf, OY2Hf2, OYHf3 and OHf4). However, a larger number of resonances are observed. As discussed in detail in Ref. 24, DFT calculations on a set of structural models reveal that there is significant overlap of the range of shifts predicted for different environments, hindering accurate decomposition and a definitive assignment of the spectral lineshape.

As x decreases from 2 to 1.8, a new signal is observed at ~230 ppm (see inset in Figure 7). As shown in Figure 8a, DFT calculations on the pyrochlore models discussed above suggest that this results from substitution of Hf into the B site in $Y_2Sn_2O_7$, creating OY2SnHf environments, predicted to have $<\delta_{iso}> \approx$ ~250 ppm and $<C_Q> \approx$ ~3.2 MHz. Although the lineshape has few discernable features characteristic of quadrupolar broadening, the width of the line (and relatively low level of substitution, and therefore relatively little broadening resulting from disorder) is not inconsistent with the C_Q values predicted. An additional resonance is also seen in the experiments at ~383 ppm (see inset in Figure 7), which can be attributed to OY4 environments with one Hf next next nearest neighbour (*i.e.*, on the closest B sites). As shown in the Supporting Information, DFT calculations predict a small decrease (~0.3 ppm) in δ_{iso} per Hf substituted onto NNNN sites. The increase in linewidth resulting from increased disorder limits the resolution of further peaks as x decreases. For x = 1.8, there is no evidence for signal that could be attributed to OY2Hf2 environments (predicted in Figure 8a to be at ~300 ppm). If a random distribution of Hf into $Y_2Sn_2O_7$ was assumed, simple statistics shows that for x = 1.8 a ratio of 90.25 : 9.5 : 0.25 for OY2Sn2 : OY2SnHf : OY2Hf2 environments would be expected. This confirms that signal from OY2Hf2 should not be observable at the signal-to-noise levels obtained, but the experimental ratio of ~14 : 1 (as opposed to the ~9.5 : 1 expected) for OY2Sn2 : OY2SnHf suggests that less Hf (estimated to be ~4%) is substituted

into this phase than expected from the nominal starting composition, in good agreement with the results from [89]Y NMR and the results shown in Figure 4b.

Figure 8a predicts that C_Q values for the different oxygen environments vary from ~0 (for OY4) to ~3.5 MHz for OY2Sn2. While the small value associated with the very symmetrical O1 site is not unexpected, it is perhaps more surprising that the C_Q values for OY2Hf2 and OY2Sn2 are so different, and that the latter is larger than the arguably less symmetrical OY2SnHf environment.[9-11] Figure S2.7 in the Supporting Information shows this difference in C_Q does not arise from any distortion/asymmetry in the local environment (with very similar distortion indices for OY2SnHf and OY2Sn2 (and OY2Hf2) environments), but is a result of the increased covalency (and consequent directionality) of the Sn-O bonding.

The peak at ~230 ppm grows with decreasing x (and increasing Hf content); however it is difficult to use the relative intensity of this peak to determine the composition of the pyrochlore phase, owing to the presence of peaks associated with the defect fluorite phase in the spectrum. These are clearly visible between 400 and 250 ppm at x = 1.2, and can be seen at a low level for x = 1.6 and (at an even lower level) for x = 1.8 (see Figure S6.2 in the Supporting Information for an expansion), again confirming the presence of a significant two-phase region in the system. Although the appearance of the defect fluorite signals seen in the $Y_2Hf_2O_7$ end member varies relatively little as the Sn content increases, there is a small increase in relative intensity for the peaks at higher δ, consistent with Sn substitution primarily for Hf.[24] To predict where peaks associated with Sn substitution into the defect fluorite phase would be observed in the spectrum further DFT calculations were carried out. The lowest energy structure from the 34 $Y_2Hf_2O_7$ models was chosen and four further structures were produced by substitution of one Hf species with Sn, leading to OY3Sn, OY2HfSn, OYHf2Sn and OHf3Sn environments. As [119]Sn spectra confirm that only six-coordinate Sn is present, in each case a six-coordinate Hf species was replaced by Sn. Figure 8b plots calculated [17]O δ_{iso} values for all O species in these models, separated by the number of Y neighbours. It can be seen that very similar δ_{iso} values (of ~ 250-220 ppm) are

16

seen for OX3Sn environments (where X is either Y or Hf), in contrast to the much broader range of shifts observed for OX4 environments. These calculations suggest that Sn substitution into $Y_2Hf_2O_7$ leads to a relatively narrow signal at lower shift that will overlap with signal from OY2SnHf species within the pyrochlore phase, again complicating any quantitative analysis of the fractions of the two phases present. An ^{17}O MQMAS NMR spectrum of $Y_2Sn_{0.6}Hf_{1.4}O_7$ (see Figure S6.3 in the Supporting Information) confirms that the width of signal seen at ~230 ppm results from a distribution of chemical shifts (and therefore chemical environments) rather than any significant increase in quadrupolar broadening (with values of $<\delta_{iso}> \approx$ ~238 ppm and $<P_Q> \approx$ ~2.6 MHz extracted from the spectrum, in reasonably good agreement with calculation). Due to the overlap of signals from different local environments in the defect fluorite phase, and the overlap of these signals with those from the pyrochlore phase and the presence of a small level of quadrupolar broadening make it too difficult to extract more quantitative structural information from the ^{17}O MAS NMR spectra. As the Hf content of the defect fluorite phase increases, the signal at $\delta \approx 165$ ppm also broadens suggesting that this too results from the overlap of signals from both pyrochlore and defect fluorite phases. Although, in principle, information is available on the composition and cation distribution within the defect fluorite phase from the spectral intensities, the overlap of signals from the two phases, the overlap of signals from centrebands (for species such as OXSn3 and OSn4) and spinning sidebands of signals in the same phase, the contribution of the ST (and need to determine this from simulation knowing an accurate C_Q value) and additional complications that could arise from non uniform enrichment between phases or species make this too challenging.

The NMR spectra of $Y_2Hf_{2-x}Sn_xO_7$, are consistent with the presence of a significant two-phase region across much of the compositional series. There is evidence in these spectra for small amounts of pyrochlore phase when x = 0.4, and for the presence of some defect fluorite phase as soon as Hf is substituted (*i.e.*, x = 1.8). However, as shown in Figure 4, the phases formed have very different compositions; there is a limited solid solution of Hf in the stannate pyrochlore (of ~10%,) no matter what the composition of the starting

materials (leading to very little change in the spectra of this phase with starting composition). In contrast, there is a much more significant, and fairly systematic, change in the composition of the co-existing defect fluorite phase. This results in much more pronounced changes with composition in the spectral lineshapes observed for this phase. This picture is similar to that seen in previous work for $Y_2Zr_{2-x}Sn_xO_7$,[19] where two phases were observed using ^{89}Y NMR for nominal values of x between 0.8 and 1.8. Combining the information from the ^{89}Y and ^{119}Sn NMR spectra (*i.e.*, the relative proportions of each type of environment present and the number of oxygen vacancies associated with each), it is possible to determine the average coordination number for Y, Sn and Hf, as shown in Figure 9. (Note this is plotted against the value of x determined by NMR and not that from the starting composition). The increased error bars at higher x result from the increased uncertainty in the analytical fitting of spectra where low-intensity, broader resonances are present. In $Y_2Hf_2O_7$, the average Hf coordination number is ~6.5 (with an average Y coordination of ~7.5), suggesting the oxygen vacancies are more usually associated with Hf. This contrasts with $Y_2Zr_2O_7$,[19] where the oxygen vacancies appeared relatively more disordered (with average coordination numbers of ~6.8 for Zr and ~7.2 for Y). As Sn is substituted into $Y_2Hf_2O_7$ (and x increases), the Y coordination number rises, with vacancies clearly ordering preferentially around Sn (which remains six-coordinate in all materials). There is only a small increase in the average coordination number of Hf until x = 1.2, above which the increase is greater. Some minor differences are seen when compared to $Y_2Zr_{2-x}Sn_xO_7$; a small decrease in the average Zr coordination number as x increases, and the average coordination number of Y in this solid solution is closer to 8 (see Supporting Information[19]). This suggests that the oxygen vacancies are more ordered (*i.e.*, found preferentially around Sn, then Zr, then Y). While a similar order of preference for vacancy association is seen for $Y_2Hf_{2-x}Sn_xO_7$ (*i.e.*, oxygen vacancies prefer to associate with Sn, then Hf then Y), the vacancies appear to be relatively more clustered around Hf than Zr. While little previous work has been carried out for $Y_2Hf_{2-x}Sn_xO_7$ using other analytical approaches, the good agreement in the average coordination numbers determined by NMR spectroscopy for $Y_2Zr_{2-x}Sn_xO_7$[19] with those determined from MD and XANES work,[44,45] provides confidence that the approach used in this work is sound.

Conclusions

Multinuclear NMR spectroscopy has been employed to investigate the phase distribution, composition and disorder in $Y_2Hf_{2-x}Sn_xO_7$. As was observed in previous work for $Y_2Zr_{2-x}Sn_xO_7$,[19] a significant two-phase region is seen, with a pyrochlore-like phase present from x = 0.4 - 2.0, and a disordered defect fluorite phase present as soon as Hf is substituted. However, the two phases have very different compositions, with a Sn-rich pyrochlore phase (with a solid solution limit of ~10% Hf) and a relatively Hf-rich defect fluorite phase. The [89]Y and ^{119}Sn NMR spectra show little evidence for any antisite cation disorder in the pyrochlore phase (*i.e.*, if this exists it is below the detection limit). However, for the defect fluorite phase there is preferential association of oxygen vacancies with Sn (which is only ever seen to be six-coordinate), and to some extent with Hf. In $Y_2Hf_2O_7$ itself, the average coordination numbers of Hf and Y are 6.5 and 7.5, respectively, suggesting vacancy clustering around Hf. In contrast, for $Y_2Zr_2O_7$,[19] oxygen vacancies appear relatively more disordered (with average coordination numbers of ~6.8 for Zr and ~7.2 for Y). However, as Sn is substituted into $Y_2Hf_2O_7$ the coordination numbers of Y and Hf become more similar than those of $Y_2Zr_{2-x}Sn_xO_7$,[19] suggesting that once Sn is present vacancy clustering/ordering is greater in the Zr-containing solid solution. ^{17}O NMR spectroscopy of $Y_2Hf_{2-x}Sn_xO_7$ was carried out on materials isotopically enriched post synthesis (by exchange with [17]O_2(g)), although high temperatures are required to ensure that uniform enrichment of the pyrochlore oxygen species is observed. The [17]O spectra confirm the formation of mixed metal materials, but chemical shifts appear sensitive primarily to the very local environment (*i.e.*, coordinating atoms) resulting in significant overlap of signals from co-existing pyrochlore and defect fluorite phases, hindering more quantitative analysis.

Our results highlight the role that techniques sensitive to local structure such as NMR spectroscopy can play in the analysis of disordered solids, and show the utility of first-

principles calculations in supporting experiment. We have demonstrated the potential complexity that can be present in these $A_2X_2O_7$ systems, showing that phases with differing compositions (that exhibit significant positional and compositional disorder) co-exist over a large compositional range. NMR, of course, is not the only option for studying local structure, with approaches such as pair distribution function (PDF) analysis or X-ray absorption near-edge structure (XANES) also sensitive to the short-range structure. There is, therefore, a more general need when studying disordered materials to exploit complementary approaches able to probe the longer-range and short-range environment, combining techniques with different sensitivities to different levels and types of disorder and different limitations, and exploiting both experiment and computation, to obtain the most detailed and accurate structural picture.

Supporting Information

Further information on powder X-ray diffraction measurements, DFT calculations, CSA-Amplified PASS experiments, additional NMR spectra and average coordination numbers can be found in the Supporting Information.

Acknowledgements

References

1. Kumar, M.; Raj, I. A.; Pattabiraman, R. $Y_2Zr_2O_7$ (YZ)-Pyrochlore Based Oxide as an Electrolyte Material for Intermediate Temperature Solid Oxide Fuel Cells (ITSOFCs) - Influence of Mn Addition on YZ. *Mater. Chem. Phys.* **2008**, *108*, 102-108.

2. Orera, A.; Slater, P. R. New Chemical Systems for Solid Oxide Fuel Cells. *Chem. Mater.* **2010**, *22*, 675-690.

3. Lumpkin, G. R. Ceramic Wasteforms for Actinides. *Elements* **2006**, *2*, 365-372.

4. Zhang, Y.; Stewart, M. W. A.; Carter, M. L.; Vance, E. R.; Moricca, S. Zirconolite-Rich Titanate Ceramics for Immobilisation of Actinides – Waste form/HIP Can Interactions and Chemical Durability. *J. Nucl. Mater.* **2009**, *395*, 69-74.

5. Ewing, R.; Weber, W. J.; Lian, Nuclear Waste Disposal–Pyrochlore ($A_2B_2O_7$): Nuclear Wasteform for the Immobilization of Plutonium and "Minor" Actinides. *J. Appl. Phys. Rev.* **2004**, *95*, 5949-5971.

6. Chakoumakos, B. C. Systematics of the Pyrochlore Structure Type, Ideal $A_2B_2X_6Y$. *J. Solid State Chem.* **1984**, *53*, 120-129.

7. Kennedy, B. J. Structural Trends in Pyrochlore Oxides. *Mater. Sci. Forum* **1996**, *228*, 753-758.

8. Subramanian, M. A.; Aravamudan, G.; Subba Rao, G. V. Oxide Pyrochlores - a Review. *Prog. Solid State Chem.* **1983**, *15*, 55-143.

9. Apperley, D. C.; Harris, R. K.; Hodgkinson, P. *Solid State NMR Basic Principles and Practice*, Momentum Press, New York, 2012.

10. Ashbrook, S. E.; Dawson, D. M.; Griffin, J. M. Solid-State Nuclear Magnetic Resonance Spectroscopy. In *Local Structure Characterisation*; Bruce, D. W., O'Hare, D., Walton, R. I., Eds.; John Wiley & Sons Ltd, **2014**; 1-88.

11. Moran, R. F.; Dawson, D. M.; Ashbrook, S. E. Exploiting NMR Spectroscopy for the Study of Disorder in Solids. *Int. Rev. Phys. Chem.* **2017**, *35*, 39-115.

12. Bonhomme, C.; Gervais, C.; Babonneau, F.; Coelho, C.; Pourpoint, F.; Azais, T.; Ashbrook, S. E.; Griffin, J. M.; Yates, J. R.; Mauri F.; Pickard, C. J. First-Principles

Calculation of NMR Parameters Using the Gauge Including Projector Augmented Wave Method: A Chemist's Point of View. *Chem. Rev.* **2012**, *112*, 5733-5779.

13. Martineau, C.; Senker J.; Taulelle, F. NMR Crystallography, *Annu. Rep. NMR Spectrosc.* **2014**, *82*, 1-57.

14. Ashbrook, S. E.; McKay, D. Combining Solid-State NMR Spectroscopy with First-Principles Calculations – a Guide to NMR Crystallography. *Chem. Commun.* **2016**, *52*, 7186-7204.

15. Reader, S. W.; Mitchell, M. R.; Johnston, K. E.; Pickard, C. J.; Whittle, K. R.; Ashbrook, S. E. Cation Disorder in Pyrochlore Ceramics: [89]Y MAS NMR and First-Principles Calculations. *J. Phys. Chem. C* **2009**, *113*, 18874-18883.

16. Mitchell. M. R.; Reader, S. W.; Johnston, K. E.; Pickard, C. J.; Whittle K. R., Ashbrook, S. E. ^{119}Sn MAS NMR and First-Principles Calculations for the Investigation of Disorder in Stannate Pyrochlores. *Phys. Chem. Chem. Phys.* **2011**, *13*, 488-497.

17. Mitchell, M. R.; Carnevale, D.; Orr, R.; Whittle K. R.; Ashbrook, S. E. Exploiting the Chemical Shielding Anisotropy to Probe Structure and Disorder in Ceramics: [89]Y MAS NMR and First-Principles Calculations. *J. Phys. Chem. C* **2012**, *116*, 4273-4286.

18. Moran, R. F.; McKay, D.; Tornstrom, P. C.; Aziz, A.; Fernandes, A.; Grau-Crespo R.; Ashbrook, S. E. Ensemble-Based Modelling of the NMR Spectra of Solid Solutions: Cation Disorder in $Y_2(Sn,Ti)_2O_7$. *J. Am. Chem. Soc.* **2019**, *141*, 17838-17846.

19. Ashbrook, S. E.; Mitchell, M. R.; Sneddon, S.; Moran, R. F.; de los Reyes, M.; Lumpkin G. R.; Whittle, K. R. New Insights into Phase Distribution, Phase Composition and Disorder in $Y_2(Zr,Sn)_2O_7$ Ceramics from NMR Spectroscopy. *Phys. Chem. Chem. Phys.* **2015**, *17*, 9049-9059.

20. Fernandes, A.; McKay, D.; Sneddon, S.; Dawson, D. M.; Lawson, S.; Veazey, R.; Whittle K. R.; Ashbrook, S. E. Phase Composition and Disorder in $La_2(Sn,Ti)_2O_7$ Ceramics: New Insights from NMR Crystallography. *J. Phys. Chem. C* **2016**, *120*, 20288-20296.

21. NMR of Quadrupolar Nuclei in Solid Materials, Ed. R. E. Wasylishen, S. E. Ashbrook and S. Wimperis, John Wiley & Sons, Chichester, UK, 2012.

22. Ashbrook S. E.; Sneddon, S. New Methods and Applications in Solid-State NMR Spectroscopy of Quadrupolar Nuclei. *J. Am. Chem. Soc.* **2014**, *136*, 15440-15456.

23. Ashbrook S. E.; Smith, M. E. Solid State ^{17}O NMR - an Introduction to the Background Principles and Applications to Inorganic Materials. *Chem. Soc. Rev.* **2006**, *35*, 718-735.

24. Fernandes, A.; Moran, R. F.; Sneddon, S.; Dawson, D. M.; McKay, D.; Bignami, G. P. M.; Blanc, F.; Whittle, K. R.; Ashbrook S. E.; ^{17}O Solid-State NMR Spectroscopy of $A_2B_2O_7$ Oxides: Quantitative Isotopic Enrichment and Spectral Acquisition? *RSC Adv*. **2018**, *8*, 7089-7101.

25. Carr, H. Y.; Purcell, E. M. Effects of Diffusion on Free Precession in Nuclear Magnetic Resonance Experiments. *Phys. Rev.* **1954**, *94*, 630-638.

26. Meiboom, S.; Gill, D. Modified Spin-Echo Method for Measuring Nuclear Relaxation Times. *Rev. Sci. Instrum*. **1958**, *29*, 688-691.

27. Orr, R. M.; Duer, M. J.; Ashbrook, S. E. Correlating Fast and Slow Chemical Shift Spinning Sideband Patterns in Solid-State NMR. *J. Magn. Reson*. **2005**, *174*, 301-309.

28. Orr, R. M.; Duer, M. J. Applications of the CSA-Amplified PASS Experiment. *Solid State Nucl. Magn. Reson*. **2006**, *30*, 1-8.

29. Bak, M.; Rasmussen, J.; Nielsen, N. SIMPSON: a General Simulation Program for Solid-State NMR Spectroscopy. *J. Magn. Reson*. **2000**, *147*, 296-330.

30. Amoureux, J. P.; Fernandez, C.; Steuernagel, S. Z-Filtering in MQMAS NMR. *J. Magn. Reson. A* **1996**, *123*, 116-118.

31. Pike, K. J.; Malde, R. P.; Ashbrook, S. E.; McManus, J.; Wimperis, S. Multiple-Quantum MAS NMR of Quadrupolar Nuclei. Do Five-, Seven- and Nine-Quantum Experiments Yield Higher Resolution than the Three-Quantum Experiment? *Solid State Nucl. Magn. Reson*. **2000**, *16*, 203-215.

32. Pickard, C. J.; Mauri, F. All-Electron Magnetic Response with Pseudopotentials: NMR Chemical Shifts. *Phys. Rev. B: Condens. Matter Mater. Phys*. **2001**, *63*, 245101.

33. Clark, S. J.; Segall, M. D.; Pickard, C. J.; Hasnip, P. J.; Probert, M. J.; Refson, K.; Payne, M. C. First-Principles Methods using CASTEP. *Z. Kristallogr. - Cryst. Mater*. **2005**, *220*, 567-570.

34. Perdew, J. P.; Burke, K.; Ernzerhof, M. Generalized Gradient Approximation Made Simple. *Phys. Rev. Lett*. **1996**, *77*, 1865-1868.

35. Vanderbilt, D. Soft Self-Consistent Pseudopotentials in a Generalized Eigenvalue Formalism. *Phys. Rev. B: Condens. Matter Mater. Phys*. **1990**, *41*, 7892-7895.

36. Yates, J. R.; Pickard, C. J.; Payne, M. C.; Mauri, F. Relativistic Nuclear Magnetic Resonance Chemical Shifts of Heavy Nuclei with Pseudopotentials and the Zeroth-Order Regular Approximation. *J. Chem. Phys*. **2003**, *118*, 5746-5743.

37. Monkhorst, H. J.; Pack, J. D. Special Points for Brillouin-Zone Integrations. *Phys. Rev. B* **1976**, *13*, 5188-5192.

38. Pyykko, P., Year-2017 Nuclear Quadrupole Moments. *Mol. Phys*. **2018,** *116*, 1328-1338.

39. Grey, C. P.; Smith, M. E.; Cheetham, A. K.; Dobson, C. M.; Dupree, R. ^{89}Y MAS NMR Study of Rare-Earth Pyrochlores: Paramagnetic Shifts in the Solid State. *J. Am. Chem. Soc.* **1990**, *112*, 4670-4765.

40. Ashbrook, S. E.; Whittle, K. R.; Lumpkin, G. R.; Farnan, I. ^{89}Y Magic-Angle Spinning NMR of $Y_2Ti_{2-x}Sn_xO_7$ Pyrochlores. *J. Phys. Chem. B* **2006**, *110*, 10358-10364.

41. Kawata, K.; Maekawa, H.; Nemoto T.; Yamamura, Y. Local Structure Analysis of YSZ by ^{89}Y MAS NMR. *Solid State Ionics* **2006**, *117*, 1687-1690.

42. Grey, C. P.; Dobson, C. M.; Cheetham, A. K.; Jakeman, R. J. B. Studies of Rare-Earth Stannates by ^{119}Sn MAS NMR. The Use of Paramagnetic Shift Probes in the Solid State. *J. Am. Chem. Soc*. **1989**, *111*, 505-511.

43. Brisse F.; Knop, O. Pyrochlores. III. X-Ray, Neutron, Infrared, and Dielectric Studies of $A_2Sn_2O_7$ Stannates, *Can. J. Chem*. **1968**, *46*, 859-873.

44. de los Reyes, M.; Whittle, K. R.; Zhang, Z.; Ashbrook, S. E.; Mitchell, M. R.; Jang L. Y.; Lumpkin, G. R. The pyrochlore to defect fluorite phase transition in $Y_2Sn_{2-x}Zr_xO_7$. *RSC Adv*. **2013**, *3*, 5090-5099.

45. Zhang, Z.; Middleburgh, S. C.; de los Reyes, M.; Lumpkin, G. R.; Kennedy, B. J.; Blanchard, P. E. R.; Reynolds E.; Jang, L. Y. Gradual Structural Evolution from Pyrochlore to Defect-Fluorite in $Y_2Sn_{2-x}Zr_xO_7$: Average vs Local Structure**.** *J. Phys. Chem. C* **2013**, 117, 26740-26749.

46. Moran, R. F.; Fernandes, A.; Dawson, D. M.; Sneddon, S.; Gandy, A.; Reeves-McLaren, N.; Whittle, K. R.; Ashbrook, S. E. Phase Distribution, Composition and Disorder in $Y_2(Hf,Sn)_2O_7$ Ceramics: Insights from Solid-State NMR Spectroscopy and First-Principles

Calculations. Dataset; University of St Andrews Research Portal, DOI: https://doi.org/10.17630/7b573f2c-1e08-45f7-9d62-a4b9c4d494a6, 2020.

Tables

Table 1. [89]Y NMR parameters (isotropic chemical shifts, δ_{iso}, relative intensities, coordination number (CN) and assignment of the resonances observed in [89]Y MAS NMR spectra of $Y_2Hf_{2-x}Sn_xO_7$ shown in Figure 2. Typical errors are estimated to be ±0.5 ppm and ±3%, except for x = 1.8 and 1.6 where the numbers shown in brackets reflect the values obtained from different fits.

Compound	δ_{iso} (ppm)	Intensity (%)	CN	Phase*	NNN
$Y_2Sn_2O_7$	147.9	100.0	8	pyr	Sn6
$Y_2Hf_{0.2}Sn_{1.8}O_7$	147.9	45.8 (58.2)	8	pyr	Sn6
	124.9	9.7 (12.3)	8	pyr	Sn5Hf
	102.9	1.7 (2.2)	8	pyr	Sn4Hf2
	142.7	33.2 (21.1)	8	df	
	239.2	9.6 (6.1)	7	df	
$Y_2Hf_{0.4}Sn_{1.6}O_7$	147.9	33.8 (45.7)	8	pyr	Sn6
	125.2	12.4 (16.7)	8	pyr	Sn5Hf
	102.9	1.6 (2.2)	8	pyr	Sn4Hf2
	123.2	34.5 (23.4)	8	df	
	223.5	17.8 (12.0)	7	df	
$Y_2Hf_{0.6}Sn_{1.4}O_7$	147.9	24.6	8	pyr	Sn6
	125.1	11.5	8	pyr	Sn5Hf
	103.2	2.8	8	pyr	Sn4Hf2
	113.9	43.1	8	df	
	214.2	17.9	7	df	
$Y_2Hf_{0.8}Sn_{1.2}O_7$	147.9	18.2	8	pyr	Sn6
	125.3	11.0	8	pyr	Sn5Hf
	103.4	2.6	8	pyr	Sn4Hf2
	112.7	43.5	8	df	
	207.5	24.7	7	df	

Y_2HfSnO_7	148.9	11.0	8	pyr	Sn6
	125.5	7.6	8	pyr	Sn5Hf
	103.8	2.1	8	pyr	Sn4Hf2
	109.1	51.9	8	df	
	204.0	27.5	7	df	
$Y_2Hf_{1.2}Sn_{0.8}O_7$	149.9	8.1	8	pyr	Sn6
	126.6	3.7	8	pyr	Sn5Hf
	103.3	0.7	8	pyr	Sn4Hf2
	97.4	52.0	8	df	
	196.9	35.5	7	df	
$Y_2Hf_{1.4}Sn_{0.6}O_7$	148.9	1.5	8	pyr	Sn6
	126.5	2.2	8	pyr	Sn5Hf
	103.9	0.3	8	pyr	Sn4Hf2
	97.7	52.7	8	df	
	198.0	42.6	7	df	
	307.0	0.9	6	df	
$Y_2Hf_{1.6}Sn_{0.4}O_7$	148.9	2.5	8	pyr	Sn6
	127.2	0.5	8	pyr	Sn5Hf
	103.9	0.1	8	pyr	Sn4Hf2
	100.5	48.6	8	df	
	197.5	47.4	7	df	
	300.0	0.9	6	df	
$Y_2Hf_{1.8}Sn_{0.2}O_7$	88.5	50.6	8	df	
	196.0	47.1	7	df	
	289.0	2.36	6	df	
$Y_2Hf_2O_7$	85.7	51.0	8	df	
	190.7	46.8	7	df	
	279.9	2.1	6	df	

* pyr = pyrochlore, df = defect fluorite

Table 2. ^{119}Sn NMR parameters (isotropic chemical shifts, δ_{iso}, relative intensities (expressed as a %), coordination number (CN) and assignment of the resonances observed in ^{119}Sn MAS NMR spectra of $Y_2Hf_{2-x}Sn_xO_7$ shown in Figure 5. Errors are estimated to be ±0.5 ppm and ±3%.

Compound	δ_{iso} (ppm)	Intensity (%)	CN	Phase*	NNN
$Y_2Sn_2O_7$	−582.6	100	6	pyr	Sn6
$Y_2Hf_{0.2}Sn_{1.8}O_7$	−582.7	77.1	6	pyr	Sn6
	−587.8	15.6	6	pyr	Sn5Hf
	−591.9	1.9	6	pyr	Sn4Hf2
	−591.2	5.4	6	df	
$Y_2Hf_{0.4}Sn_{1.6}O_7$	−582.8	57.5	6	pyr	Sn6
	−587.8	28.5	6	pyr	Sn5Hf
	−593.1	2.4	6	pyr	Sn4Hf2
	−594.3	11.6	6	df	
$Y_2Hf_{0.6}Sn_{1.4}O_7$	−582.7	54.7	6	pyr	Sn6
	−587.8	21.7	6	pyr	Sn5Hf
	−592.9	4.8	6	pry	Sn4Hf2
	−592.7	18.8	6	df	
$Y_2Hf_{0.8}Sn_{1.2}O_7$	−583.1	41.2	6	pyr	Sn6
	−588.2	22.5	6	pyr	Sn5Hf
	−593.4	6.6	6	pyr	Sn4Hf2
	−595.1	29.6	6	df	
Y_2HfSnO_7	−583.1	26.9	6	pyr	Sn6
	−588.2	25.7	6	pyr	Sn5Hf
	−593.4	6.4	6	pyr	Sn4Hf2
	−601.1	41.1	6	df	
$Y_2Hf_{1.2}Sn_{0.8}O_7$	−582.9	2.6	6	pyr	Sn6
	−588.2	3.0	6	pyr	Sn5Hf
	−602.9	94.5	6	df	

$Y_2Hf_{1.4}Sn_{0.6}O_7$	−582.2	1.7	6	pyr	Sn6
	−604.3	98.3	6	df	
$Y_2Hf_{1.6}Sn_{0.4}O_7$	−607.8	100	6	df	
$Y_2Hf_{1.8}Sn_{0.2}O_7$	−615.9	100	6	df	

* pyr = pyrochlore, df = defect fluorite

Figure captions

Figure 1. Structure of a typical $A_2B_2O_7$ (a) pyrochlore and (b) defect fluorite (shown as a $2 \times 2 \times 2$ supercell) material. Also shown are expansions of the local environments of (a) the 16c (A), 16d (B), 8a (O1) and 48f (O2) sites, and (b) the 4a (cation) and 8c (anion) sites. Note that in (b), 1/8 of all anion sites are vacant.

Figure 2. ^{89}Y (14.1 T, 14 kHz) MAS NMR spectra of $Y_2Hf_{2-x}Sn_xO_7$. The asterisk (*) denotes a small unknown impurity in some of the samples.

Figure 3. Plots showing calculated (using DFT) ^{89}Y δ_{iso} for (a) defect fluorite structural models of $Y_2Hf_2O_7$ against Y coordination number and (b) pyrochlore models of $Y_2(Hf,Sn)_2O_7$ against the number n of Sn NNN. See the Supporting Information for a description of the NNN environments denoted in (b).

Figure 4. Plot showing (a) the amount of pyrochlore (pyr) and defect fluorite (df) phases, (b) the composition of the two phases and (c) the relative proportions of each type of Sn/Hf, as a function of nominal composition. In (b), the percentages of the Sn and Hf in the pyrochlore phase (and in the defect fluorite phase) should equal 100%. In (c), the percentage of Sn in the pyrochlore and defect fluorite phases should add to 100%. Error bars are estimated from different fits. When these are not shown they are smaller than the data points.

Figure 5. ^{119}Sn (9.4 T, 14 kHz) MAS NMR spectra of $Y_2Hf_{2-x}Sn_xO_7$. The asterisks (*) denote spinning sidebands.

Figure 6. Plots showing calculated (using DFT) ^{119}Sn δ_{iso} for pyrochlore models of $Y_2(Hf,Sn)_2O_7$ against (a) the number n of Sn NNN and (b) Sn coordination number (for pyrochlore models where oxygen atoms have been moved from 8a to vacant 8b sites

thereby changing the Sn coordination number). See the Supporting Information for a description of the NNN environments denoted in (a).

Figure 7. ^{17}O (14.1 T, 21 kHz) MAS NMR spectra of $Y_2Hf_{2-x}Sn_xO_7$, enriched at 900 °C for 12 h. The asterisks (*) denote spinning sidebands.

Figure 8. Plots showing (a) calculated ^{17}O NMR parameters (δ_{iso} and C_Q) for pyrochlore models of $Y_2(Hf,Sn)_2O_7$ and (b) calculated ^{17}O δ_{iso} for defect fluorite models of $Y_2Hf_2O_7$ with substitution of one Sn.

Figure 9. Plot showing the variation in average coordination number of Y, Sn and Hf in the disordered defect fluorite phase as a function of the actual (not nominal) composition (as shown in Figure 4b).

Figure 1

Figure 2

x = 2.0

x = 1.8

x = 1.6

x = 1.4

x = 1.2

x = 1.0

x = 0.8

x = 0.6

x = 0.4

x = 0.2

x = 0.0

300 200 100 0
δ (ppm)

300 200 100 0
δ (ppm)

Figure 3

Figure 4

a

b

c
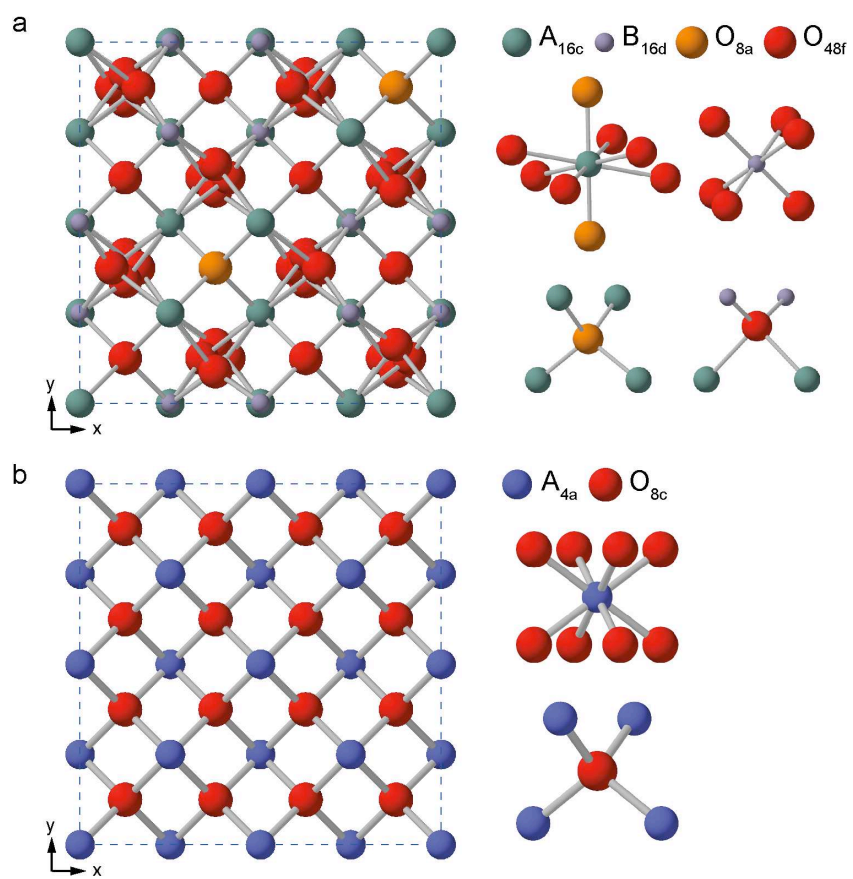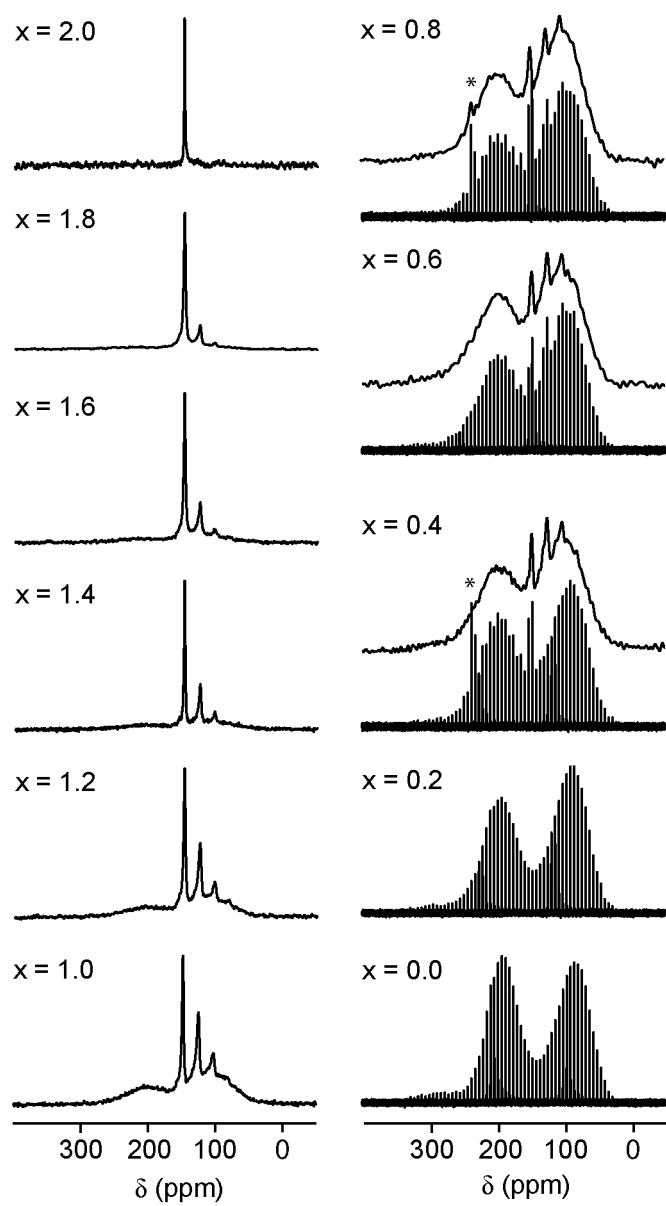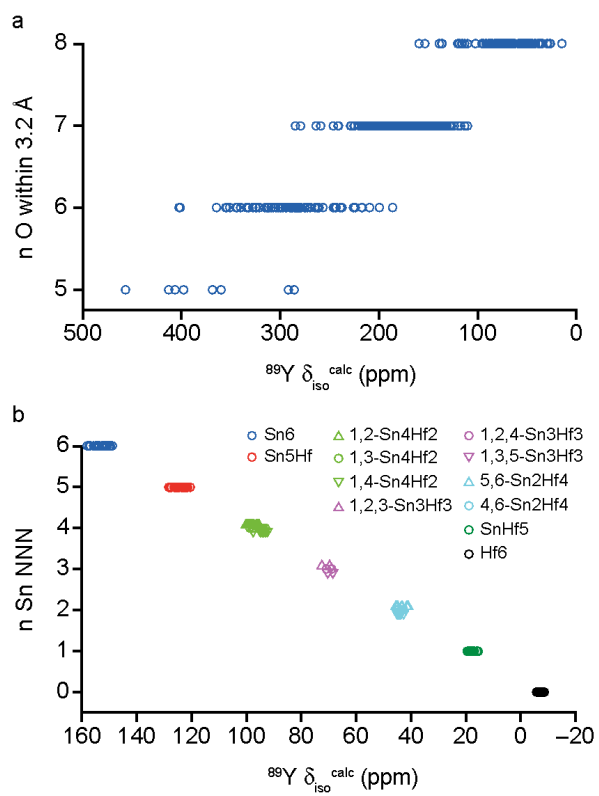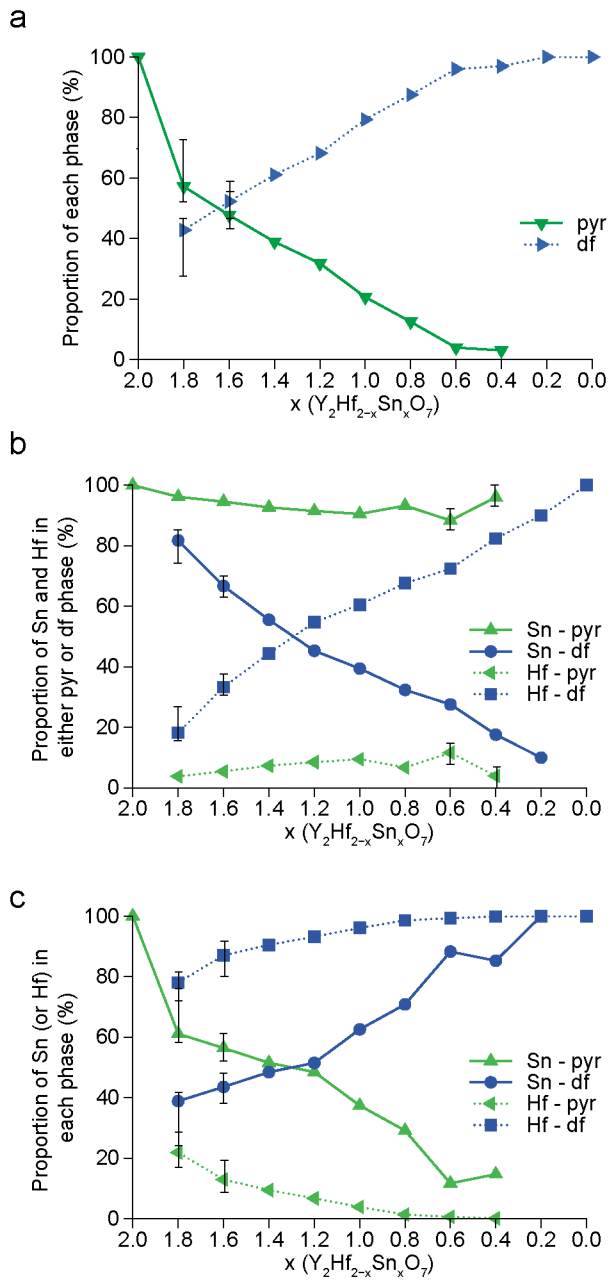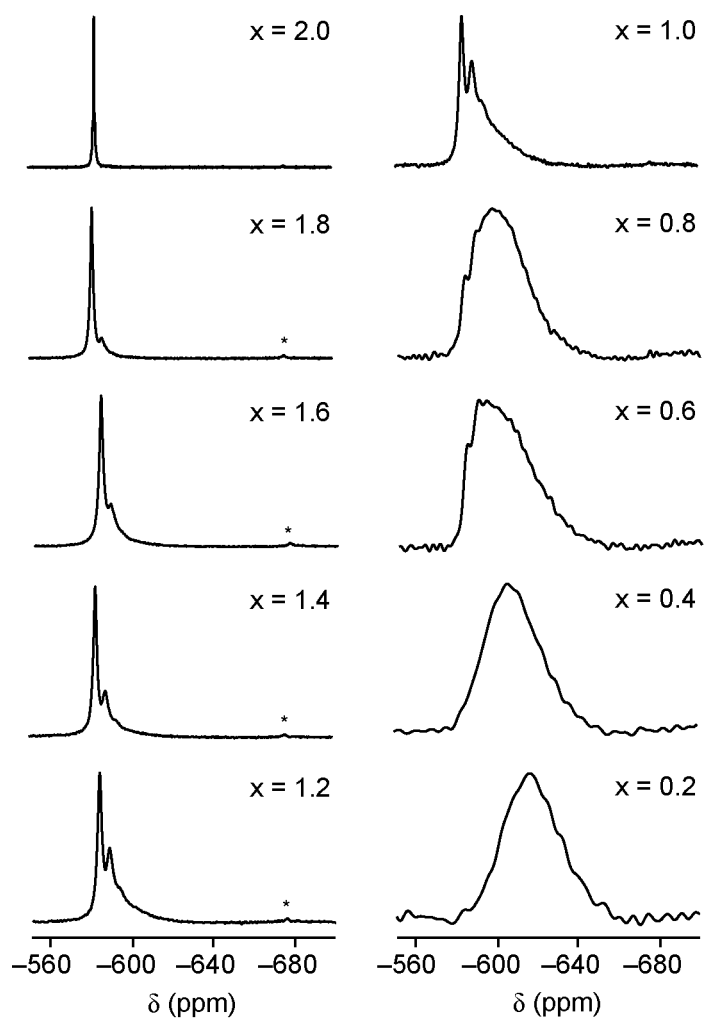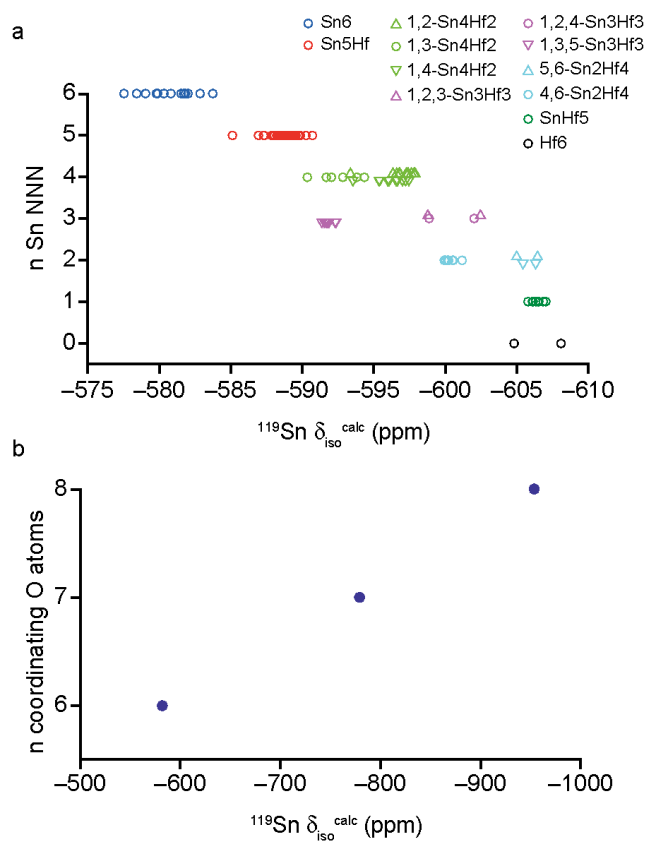
Figure 5

Figure 6

Figure 7
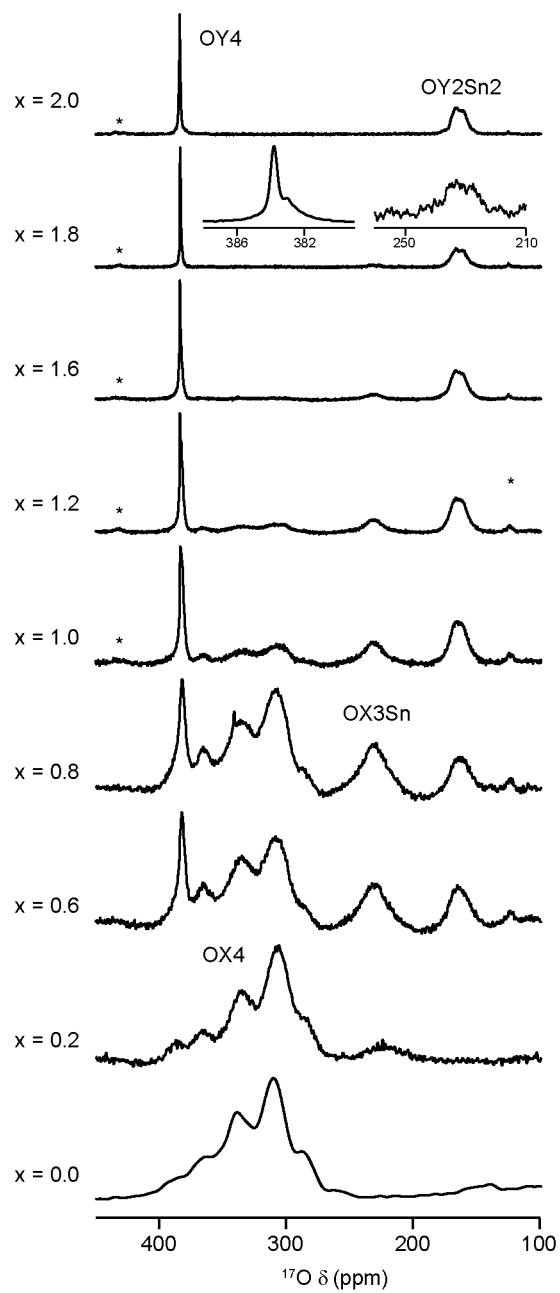
Figure 8
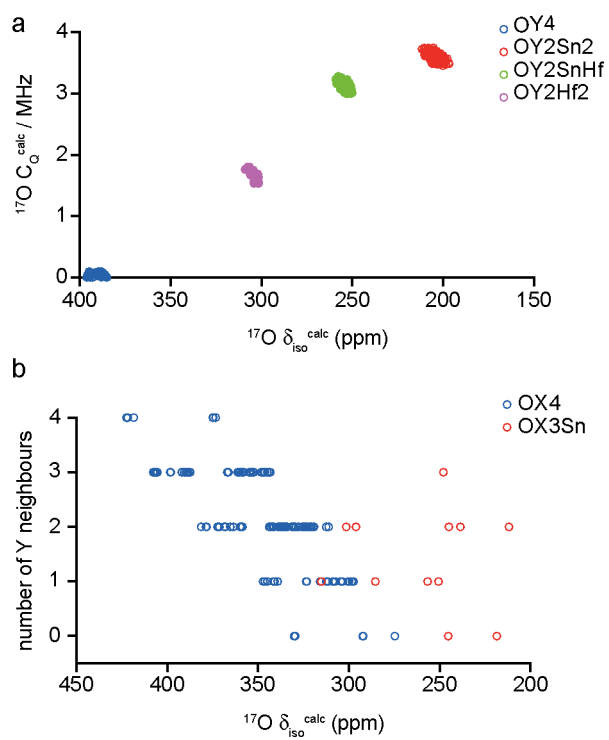
Figure 9
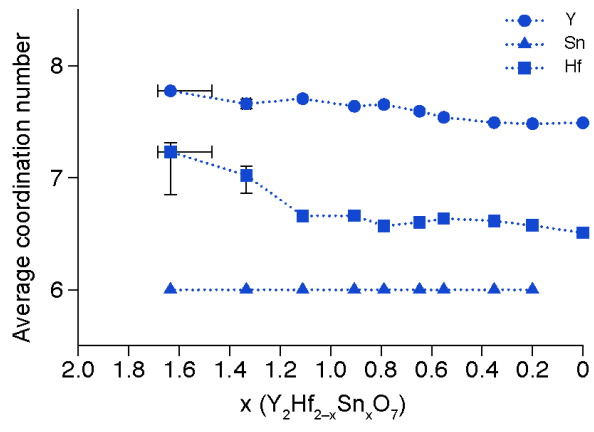
TOC graphic

Phase Distribution, Composition and Disorder in $Y_2(Hf,Sn)_2O_7$ Ceramics: Insights from Solid-State NMR Spectroscopy and First-Principles Calculations

Robert F. Moran,[1] Arantxa Fernandes,[1] Daniel M. Dawson,[1] Scott Sneddon,[1]
Amy S. Gandy,[2] Nik Reeves-McLaren,[2] Karl R. Whittle[2,3]
and Sharon E. Ashbrook,[1]*

[1]*School of Chemistry, EaStCHEM and Centre of Magnetic Resonance, University of St Andrews, St Andrews KY16 9ST, United Kingdom*

[2]*Department of Materials Science and Engineering, University of Sheffield, Mappin Street, Sheffield S1 3JD, UK*

[3]*School of Engineering, University of Liverpool, Brownlow Hill, Liverpool, L69 3GH, UK*

Supporting Information

S1. Powder X-ray diffraction measurements

S2. Further information on DFT calculations

S3. CSA-amplified PASS experiments

S4. Further information on ^{89}Y MAS NMR spectra

S5. Further information on ^{119}Sn MAS NMR spectra

S6. Further information on ^{17}O MAS NMR spectra

S7. Comparison of average coordination numbers in defect fluorite phases

S8. References

S1. Powder X-ray diffraction measurements

Figure S1.1 shows powder X-ray diffraction (pXRD) measurements for $Y_2Hf_{2-x}Sn_xO_7$, indicating no significant impurities are seen by diffraction.
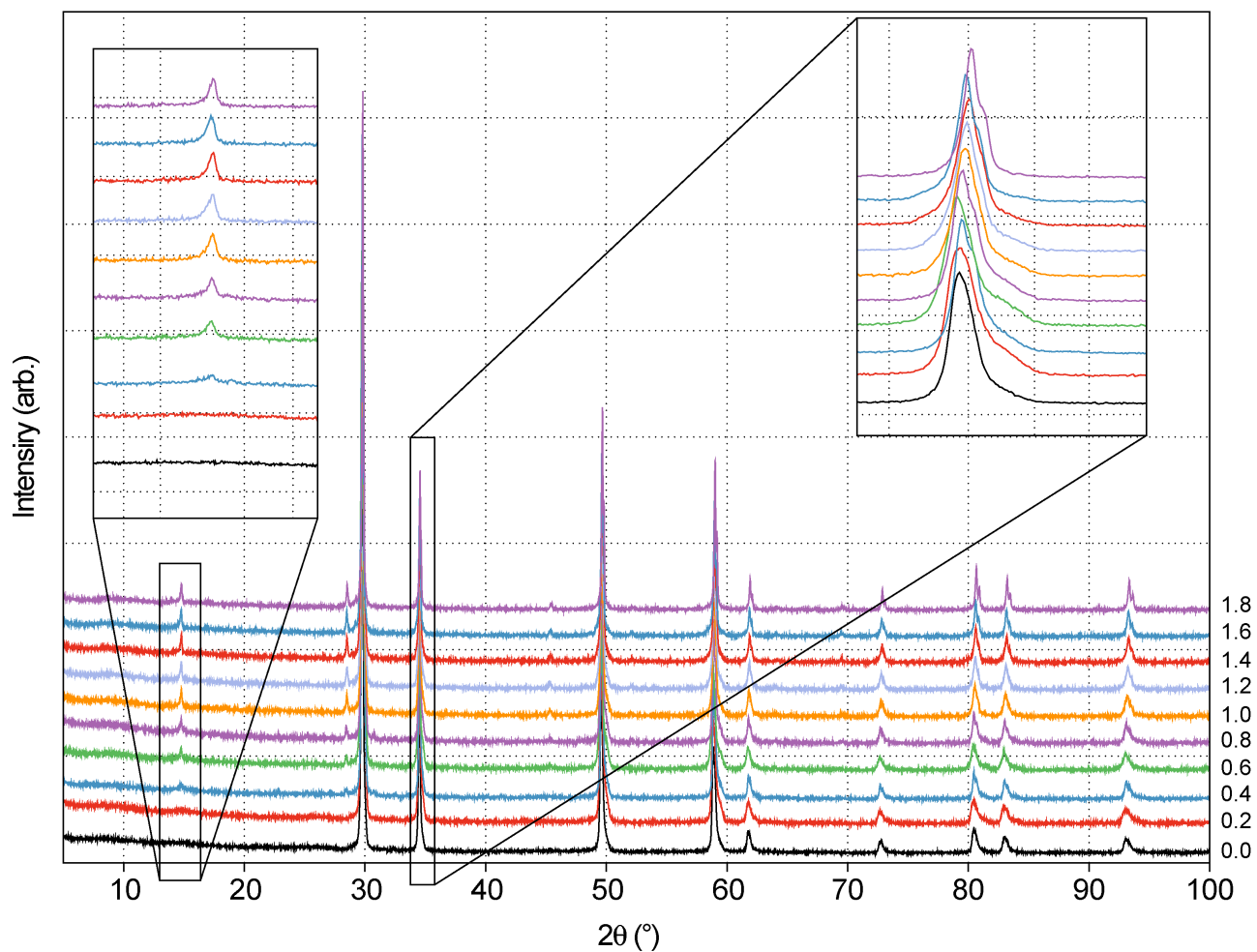
Figure S1.1. Powder XRD patterns for $Y_2Hf_{2-x}Sn_xO_7$.

S2. Further information on DFT calculations

Calculations of total energies and NMR parameters were carried out using the CASTEP density functional theory (DFT) code (version 8.0),[S1-S2] employing the gauge-including projector augmented wave (GIPAW) approach[S1] to reconstruct the all-electron wavefunction in the presence of a magnetic field. Calculations were performed using the GGA PBE functional[S3] and core-valence interactions were described by ultrasoft pseudopotentials,[S4] accounting for scalar relativistic effects using ZORA.[S5] A planewave energy cutoff of 60 Ry (~816 eV) was used, and integrals over the first Brillouin zone were performed using a Monkhorst-Pack grid[S6] with a k-point spacing of 0.04 2π Å^{-1}. All calculations were converged as far as possible with respect to both k-point spacing and energy cutoff. In the geometry optimisation all atomic coordinates and unit cell parameters were allowed to vary, with a geometry optimization energy tolerance of 1×10^{-5} eV per atom and an electronic structure energy tolerance of 1×10^{-9} eV per atom used.

Referencing

To facilitate comparison to experiment σ_{iso}^{calc} values were converted to δ_{iso}^{calc} values. For [89]Y, this was achieved by comparing experimental and calculated NMR parameters for a series of simple yttrium-containing solids, as described in Ref. S7. From the line of best fit, shown in Figure S2.1 it can be seen that

$$\delta_{iso}^{calc} = -0.9864\, \sigma_{iso}^{calc} + 2652.5547 \ . \tag{S2.1}$$

as described in Ref. S7 and shown in Figure S2.1. A [119]Sn reference shielding was determined by comparing the experimental shift of $Y_2Sn_2O_7$ (δ_{iso}^{exp} = -582 ppm[S8]) and calculated shielding (σ_{iso}^{calc} = 3183.94 ppm), giving σ_{ref} = 2601.94 ppm. δ_{iso}^{calc} is then given by

$$\delta_{iso}^{calc} = \sigma_{iso}^{calc} - \sigma_{ref} \ . \tag{S2.2}$$

For ^{17}O, an approach similar to that outlined in Ref. S9 was used (with the inclusion of one additional oxide (BaO), where experimental and calculated NMR parameters for a series of oxides were compared. The line of best fit,

$$\delta_{iso}{}^{calc} = -0.9002\ \sigma_{iso}{}^{calc} + 228.8128\ ,\qquad\qquad\qquad (S2.3)$$

is shown in Figure S2.2. Note that previous calculations were carried out with slightly lower cut off energies and k points, but as these are well converged any uncertainty in the reference shielding is estimated to e less than 1% of the shift range.
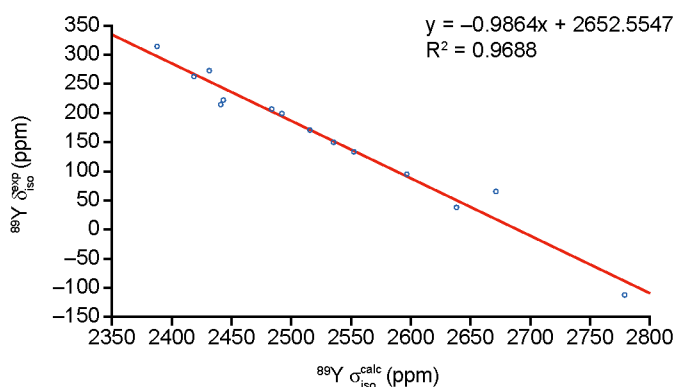
Figure S2.1. Plot of ^{89}Y experimental δ_{iso} against calculated σ_{iso} for a series of yttrium-containing compounds.[S7]
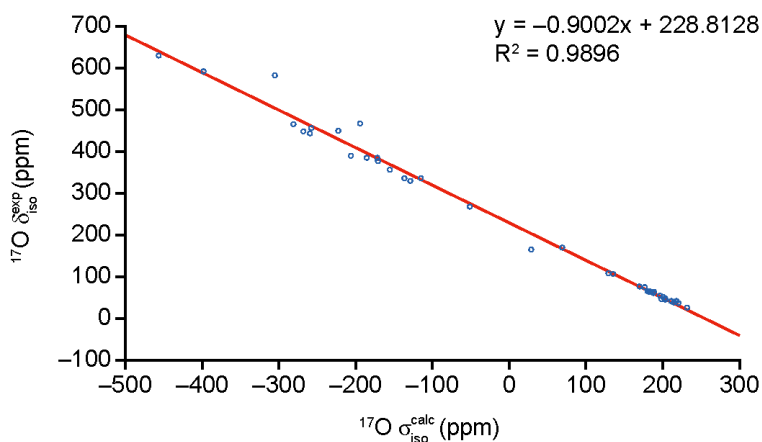
Figure S2.2. Plot of ^{17}O experimental δ_{iso} against calculated σ_{iso} for a series of oxides.[S9]

Pyrochlore models

Calculations were performed for a single unit cell of $Y_2Sn_2O_7$, where the environment of one of the Y or Sn species was modified systematically, altering both the number of the surrounding B-site cations (*i.e.*, Sn and Hf) and their spatial arrangement, as shown in Figure S2.3. In each case, the geometry of the structure was optimized (with atomic coordinates and unit cell parameters allowed to vary), prior to calculation of the NMR parameters. A similar set of calculations was performed for a hypothetical $Y_2Hf_2O_7$ pyrochlore, to enable the prediction of chemical shifts resulting from environments with a greater proportion of Hf in either the NNN or long-range environment. For the Sn centered calculations a single Sn was first placed into the $Y_2Hf_2O_7$ structure and its environment then modified as described above. This approach generated a total of 52 structural models (26 Y centered and 26 Sn centered). A further two models were created by moving firstly one, and subsequently two, 8a O species in $Y_2Sn_2O_7$ to vacant 8b sites surrounding Sn, thereby creating seven- and eight-coordinated Sn respectively. ^{119}Sn chemical shifts predicted for these models are shown in Figure 6b of the main text. Figure S2.3 shows the local atomic environments around the pyrochlore A and B sites, and the numbering scheme used to denote the different arrangements of the atoms on the six next nearest neighbour (NNN) B sites in each case.
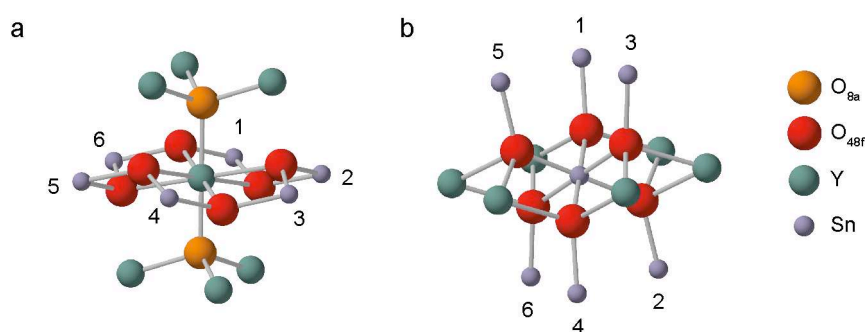
Figure S2.3. The local environment around the pyrochlore (a) A site (occupied by Y) and (b) B site (occupied by Sn or Hf), showing the numbering scheme used.

Defect fluorite models

A set of 30 $Y_2Hf_2O_7$ defect fluorite structural models was produced, starting from a $2 \times 2 \times 2$ supercell of ideal AO_2 fluorite, as described in Ref. S9. 16 of the 32 cation sites were

randomly selected to be occupied by Y, with the remainder occupied by Hf. Similarly, 8 of the 64 anion sites were randomly selected to be vacant (and the remaining 56 occupied by O). The structures were optimised using DFT. In addition, a further four structural models were considered. The first was a $Y_2Hf_2O_7$ pyrochlore structure (*i.e.*, with ordering of cations and anions) generated by atom substitution from a structural model of $Y_2Sn_2O_7$. Two models were generated from this; one by moving one 8a O to a vacant 8b site (creating a seven-coordinate Y species and an OHf_4 environment), and a second by moving another 8a O from around the same Y to a vacant 8b site (creating a six-coordinate Y species). The final structural model was a reverse pyrochlore structure, *i.e.*, containing Y on the B site and Hf on the A site. All structures were optimised. In order to gain insight into the chemical shift changes seen upon Sn substitution into $Y_2Hf_2O_7$, the lowest energy structure from the 34 $Y_2Hf_2O_7$ models discussed above was used. Distinct OY3Hf, OY2Hf2, OYHf3 and OHf4 species were manually modified by substituting a six-coordinate Hf^{4+} cation with a Sn^{4+} (as Sn has been shown to prefer to be six coordinate in this work and in previous studies) to give four separate new structural models.

Calculated shift anisotropies

Figure S2.4 shows a plot of the variation in the calculated [89]Y Ω for the 26 Y-centred pyrochlore models of $Y_2(Hf,Sn)_2O_7$ as the number n of Sn NNN varies. An increase in the average Ω of ~90 ppm with each Hf added is observed.
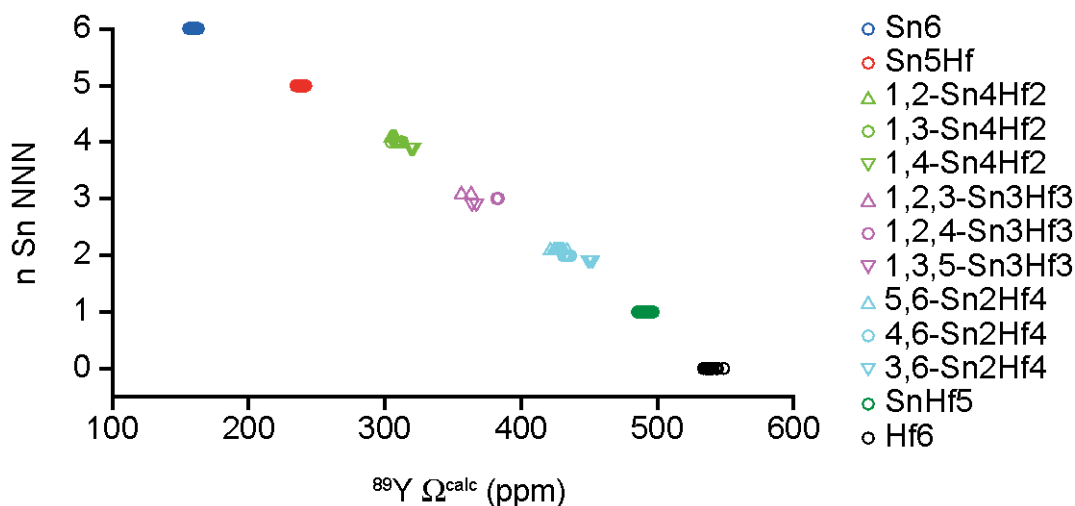
Figure S2.4. Plot showing calculated (using DFT) ^{89}Y Ω for the 26 Y-centred pyrochlore models of $Y_2(Hf,Sn)_2O_7$ with respect to the number n of Sn NNN.

Figure S2.5 shows a plot of the variation in the calculated ^{119}Sn Ω for the 26 Sn-centred pyrochlore models of $Y_2(Hf,Sn)_2O_7$ as the number n of Sn NNN varies.
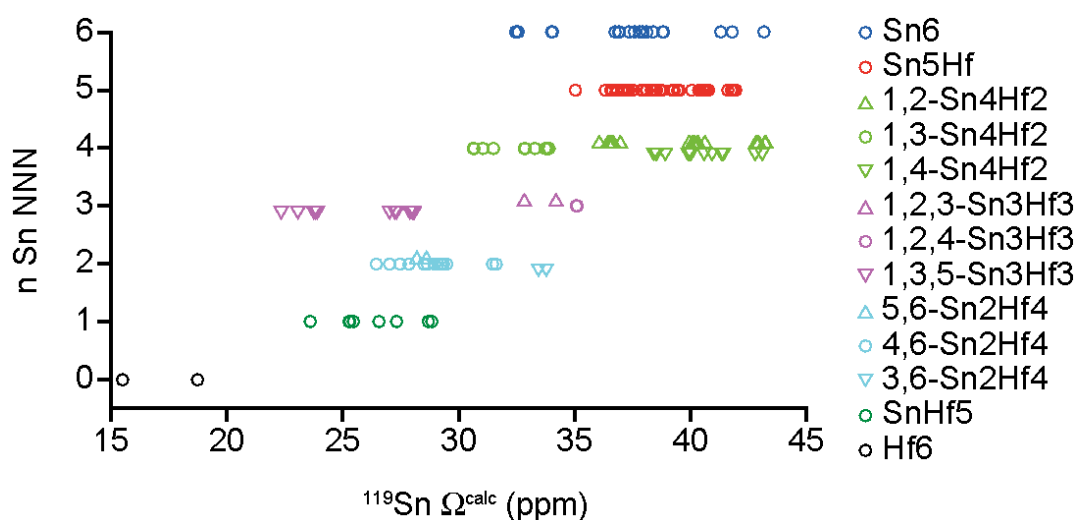
Figure S2.5. Plot showing calculated (using DFT) ^{119}Sn Ω for the 26 Sn-centred pyrochlore models of $Y_2(Hf,Sn)_2O_7$ with respect to the number n of Sn NNN.

^{17}O DFT calculations

Figure S2.6 shows calculated ^{17}O δ_{iso}^{calc} for O1 (OY4) environments in pyrochlore models of $Y_2Sn_2O_7$ and $Y_2Sn_2O_7$ substituted with 1 and 2 Hf, plotted as a function of the number of Hf species on the next next nearest neighbouring (NNNN) B sites (*i.e.,* O-Y-O-Hf linkages).

Calculations predict a small (~0.3 ppm) decrease in δ_{iso}^{calc} with increasing numbers of Hf substituted onto the B sites.
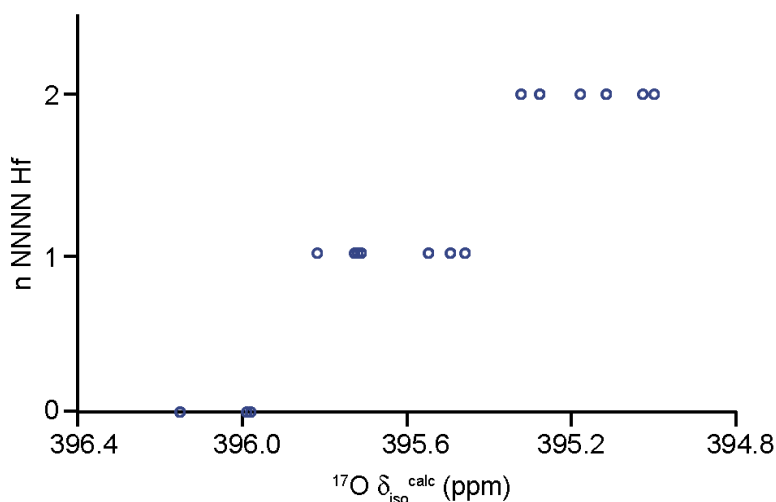
Figure S2.6. Plot showing calculated ^{17}O δ_{iso} for O1 (OY4) environments (with n Hf NNNN) in pyrochlore models of $Y_2Sn_2O_7$ and $Y_2Sn_2O_7$ substituted with one or two Hf.

Figure S2.7 shows how the calculated ^{17}O C_Q for pyrochlore models of $Y_2(Hf,Sn)_2O_7$ varies with the distortion index. The distortion index is a measure of the deviation from ideal tetrahedral coordination environment, and is given by

$$ DI = \frac{\sum_i |\theta_i - \theta_0|}{6} , \tag{S2.1} $$

where θ_0 is the ideal tetrahedral angle (109.471°). The plot shows that the variation in calculated C_Q observed between OY2Hf2, OY2Sn2 and OY2Hf2 environments does not arise from increased distortion in the local environment. This difference likely arises from the increased covalency of the Sn-O bond (in comparison to Hf-O and Y-O) that results in more directional bonding and a decrease in the symmetry of the local environment.
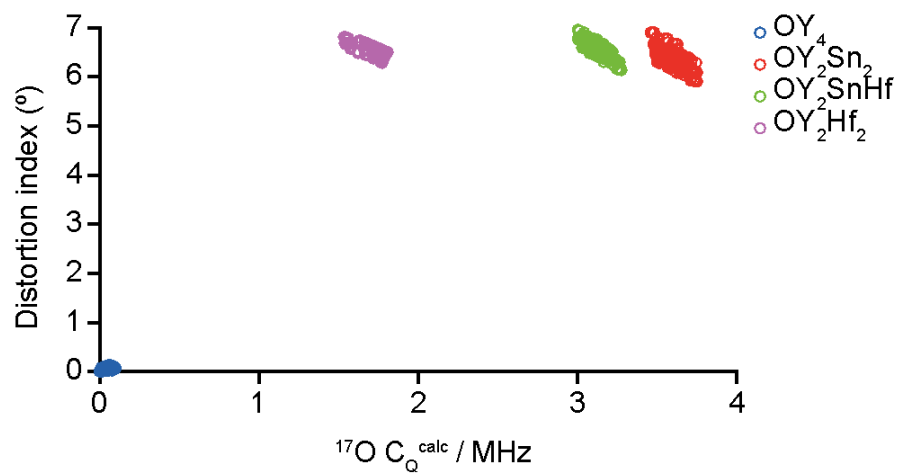
Figure S2.7. Plot showing the variation of calculated ^{17}O C_Q for pyrochlore models of $Y_2(Hf,Sn)_2O_7$ with distortion index.

S3. CSA-amplified PASS experiments

^{89}Y and ^{119}Sn two-dimensional CSA-amplified PASS NMR experiments were carried out using the pulse sequence of Orr *et al.*[S10-S11] For ^{89}Y NMR experiments, the original pulse sequence was modified to include an initial saturation train. The total scaling factor is given by $\chi_T = (n_{PASS} + 1) \chi$, where χ is the scaling factor (determined by the timing of the five π pulse blocks) and n_{PASS} is the number of additional blocks used. Cogwheel phase cycling[S12] was used in order to reduce the length of the phase cycle required. Fitting of the sideband manifold extracted from the indirect dimension of the two-dimensional CSA-amplified PASS spectrum was carried out using SIMPSON[S13] by comparison to a simulated two-dimensional CSA-amplified PASS experiment using ideal pulses for ^{119}Sn, and simulating the complete two-dimensional NMR experiment using an estimated radiofrequency field strength for ^{89}Y. The 'root mean square' (rms) error quoted in tables and plotted in figures is that outputted by SIMPSON and described in Ref. S13.

Table S3.1 gives the acquisition parameters used for ^{89}Y and ^{119}Sn two-dimensional CSA-amplified PASS NMR spectra.

Table S3.1. Acquisition parameters for ^{89}Y and ^{119}Sn two-dimensional CSA-amplified PASS experiments.

Parameter	^{89}Y	^{119}Sn
B_0 / T	14.1	9.4
MAS rate in F_1 / kHz	1.5	1.87
MAS rate in F_2 / kHz	10.0	14.0
Spectral width / kHz	24.0	29.9
Number of rows	16	16
χ_T	6.6667	7.5
χ	3.3333	2.5
n_{PASS}	2	3
Number of transients	962 – 4498	76
Recycle interval / s	10	30
Saturation delay / ms	50	
Number of saturation pulses	16	

^{89}Y CSA parameters were measured using two-dimensional CSA-amplified PASS experiments for $Y_2Hf_{2-x}Sn_xO_7$ samples with x = 2.0 to 1.0. The values extracted, along with the corresponding rms error for the fits, are given in Table S3.2. As an example, Figure S3.1 shows the ^{89}Y two-dimensional CSA-amplified PASS spectrum of $Y_2Hf_{0.4}Sn_{1.6}O_7$. Also shown are analytical fits (fitted by simulating the complete two-dimensional NMR experiment using an estimated radiofrequency field strength for ^{89}Y) and the plots of the rms error for the three spinning sideband manifolds.
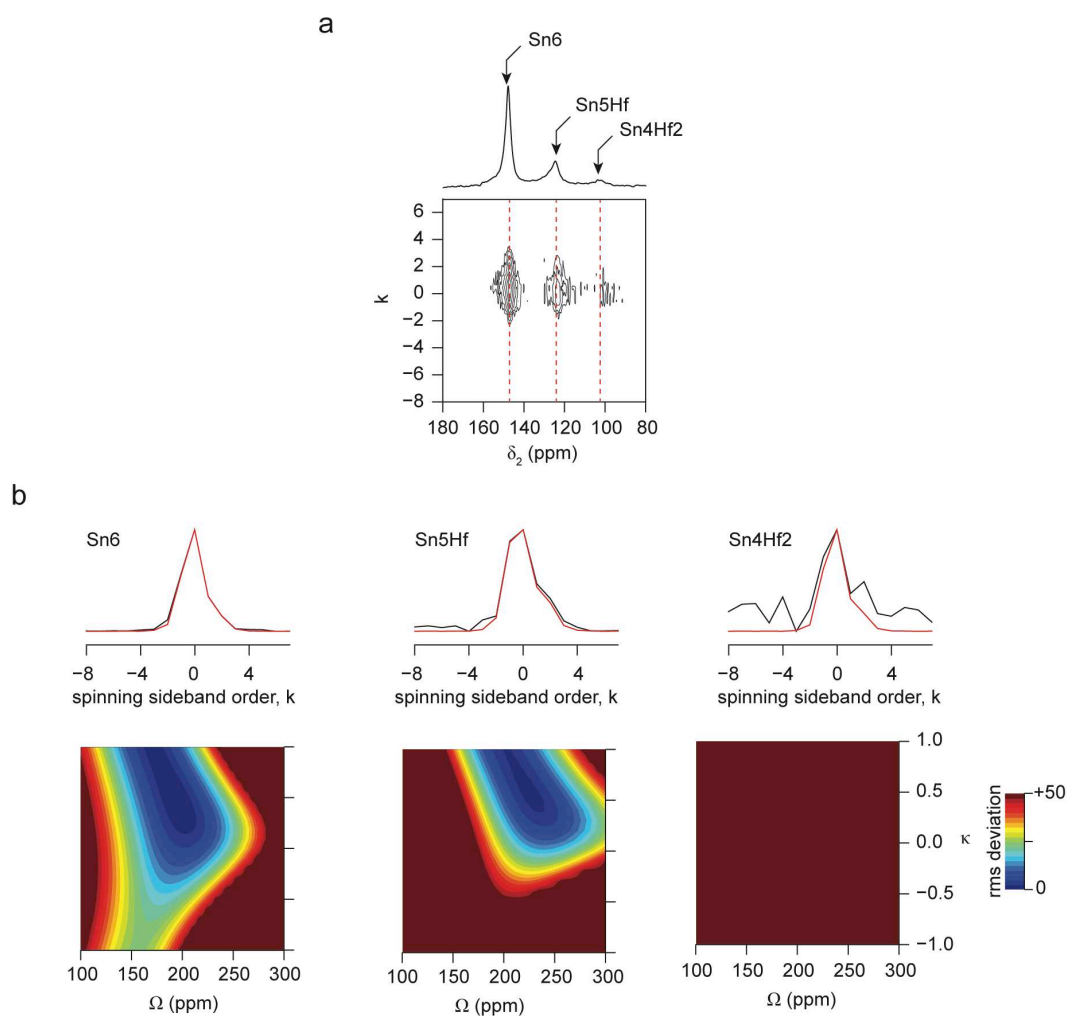
Figure S3.1 (a) ^{89}Y (14.1 T) two-dimensional CSA-amplified PASS spectrum of $Y_2Hf_{0.4}Sn_{1.6}O_7$. See Table S3.1 for experimental acquisition parameters. (b) Extracted spinning sideband manifolds for the three resonances along with their corresponding analytical fits, shown in red. Also shown are the contour plots of rms error (arbitrarily restricted from 0 to 50).

Table S3.2. Experimental ^{89}Y NMR parameters (Ω and κ) and corresponding rms error resulting from the analytical fits of the spinning sideband manifolds of the pyrochlore peaks extracted from the two-dimensional CSA-amplified PASS spectra of $Y_2Hf_{2-x}Sn_xO_7$.

Compound	δ_{iso} (ppm)[a]	Ω (ppm)	κ	rms error	NNN
$Y_2Sn_2O_7$	147.9	209 ± 13	0.5 ± 0.3	0.5	Sn6
$Y_2Hf_{0.2}Sn_{1.8}O_7$	147.9	210 ± 13	0.5 ± 0.3	0.5	Sn6
	124.9	256 ± 12	0.2 ± 0.1	9.7	Sn5Hf
	103.3				Sn4Hf2
$Y_2Hf_{0.4}Sn_{1.6}O_7$	147.9	203 ± 17	0.5 ± 0.3	0.6	Sn6
	125.2	234 ± 19	0.7 ± 0.2	1.6	Sn5Hf
	102.9				Sn4Hf2
$Y_2Hf_{0.6}Sn_{1.4}O_7$	147.9	206 ± 19	0.6 ± 0.3	0.5	Sn6
	125.1	234 ± 17	0.8 ± 0.2	5.3	Sn5Hf
	103.2	244 ± 13	0.8 ± 0.1	59.4	Sn4Hf2
$Y_2Hf_{0.8}Sn_{1.2}O_7$	147.9	198 ± 19	0.7 ± 0.3	0.8	Sn6
	125.3	227 ± 17	1.0 ± 0.2	3.1	Sn5Hf
	103.4	275 ± 13	0.8 ± 0.1	30.9	Sn4Hf2
Y_2HfSnO_7	148.9	193 ± 22	0.9 ± 0.3	1.2	Sn6
	125.5	249 ± 12	0.6 ± 0.2	7.5	Sn5Hf
	103.8	260 ± 14	0.7 ± 0.2	32.1	Sn4Hf2

[a] Errors in δ_{iso} are estimated to be ± 0.5 ppm.

^{119}Sn CSA parameters were measured using two-dimensional CSA-amplified PASS experiments for $Y_2Hf_{2-x}Sn_xO_7$ samples with x = 2.0 to 1.0. The values extracted, along with the corresponding rms error for the fits, are given in Table S3.3. As an example, Figure S3.2 shows the ^{119}Sn two-dimensional CSA-amplified PASS spectrum of $Y_2Hf_{0.4}Sn_{1.6}O_7$. Also shown are analytical fits (fitted by comparison to a simulated two-dimensional CSA-amplified PASS experiment using ideal pulses) and the plots of the rms error for the three spinning sideband manifolds.
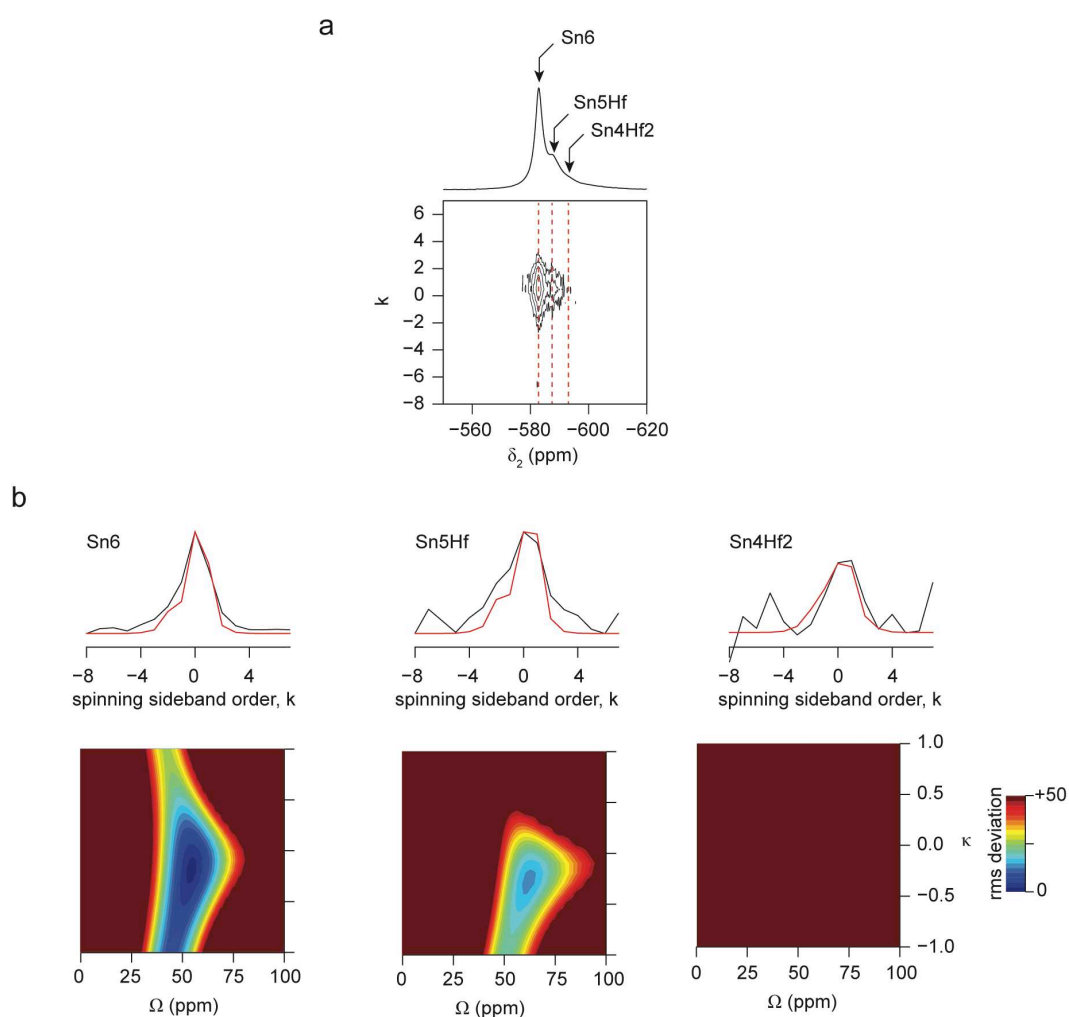
Figure S3.2 (a) ^{119}Sn (9.4 T) two-dimensional CSA-amplified PASS spectrum of $Y_2Hf_{0.4}Sn_{1.6}O_7$. See Table S3.1 for experimental acquisition parameters. (b) Extracted spinning sideband manifolds for the three resonances along with their corresponding analytical fits, shown in red. Also shown are the contour plots of rms error (arbitrarily restricted from 0 to 50).

Table S3.3. Experimental ^{119}Sn NMR parameters (Ω and κ) and corresponding rms error resulting from the analytical fits of the spinning sideband manifolds of the pyrochlore peaks extracted from the two-dimensional CSA-amplified PASS spectra of $Y_2Hf_{2-x}Sn_xO_7$.

Compound	δ_{iso} (ppm)[a]	Ω (ppm)	κ	rms error	NNN
$Y_2Sn_2O_7$	−582.6	43 ± 5	−1.0 ± 0.1		Sn6
$Y_2Hf_{0.2}Sn_{1.8}O_7$	−582.7	44 ± 3	−1.0 ± 0.2	4.7	Sn6
	−587.8	36 ± 4	−1.0 ± 0.4	25.0	Sn5Hf
$Y_2Hf_{0.4}Sn_{1.6}O_7$	−582.8	46 ± 3	−1.0 ± 0.2	7.7	Sn6
	−587.8	52 ± 4	−1.0 ± 0.2	20.0	Sn5Hf
	−593.1	62 ± 4	−0.3 ± 0.4	62.7	Sn4Hf2
$Y_2Hf_{0.6}Sn_{1.4}O_7$	−582.7	43 ± 3	−1.0 ± 0.2	1.2	Sn6
	−587.8	44 ± 3	−1.0 ± 0.2	7.5	Sn5Hf
	−592.9[b]				Sn4Hf2

[a] Errors in δ_{iso} are estimated to be ± 0.5 ppm.

[b] The intensity of this resonance is too low to extract the spinning sideband manifold.

S4. Further information on [89]Y MAS NMR spectra

Figure S4.1 shows the effect of including the broad resonances associated with the presence of a defect fluorite phase in the analytical fitting of [89]Y MAS NMR spectra of $Y_2Hf_{0.2}Sn_{1.8}O_7$.
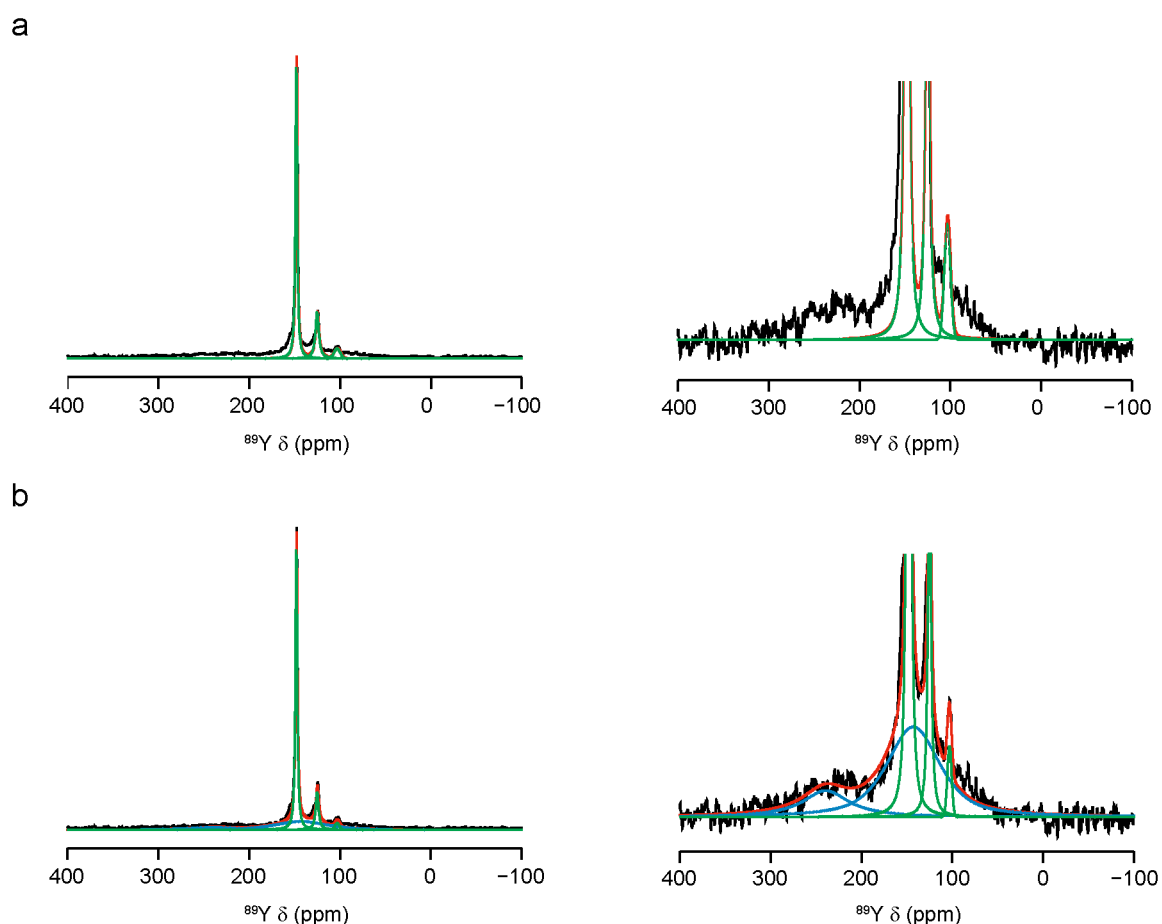
Figure S4.1. Analytical fits and corresponding (vertical) expansions of the [89]Y MAS NMR spectrum of $Y_2Hf_{0.2}Sn_{1.8}O_7$. In (a), the spectrum is fitted without the inclusion of the broad resonances associated with the disordered defect fluorite phase. In (b), two broad resonances are included. The green, blue and red lines denote the analytical fit for the pyrochlore phase, defect fluorite phase and all resonances, respectively.

From a fitting of each of the [89]Y MAS NMR spectra of $Y_2Hf_{2-x}Sn_xO_7$ in Figure 2 of the main text, the chemical shifts of the individual components, and their relative intensities can be

extracted. These are given in Table 1 (main text) and shown in Figure S4.2 as a function of the composition of the starting materials.
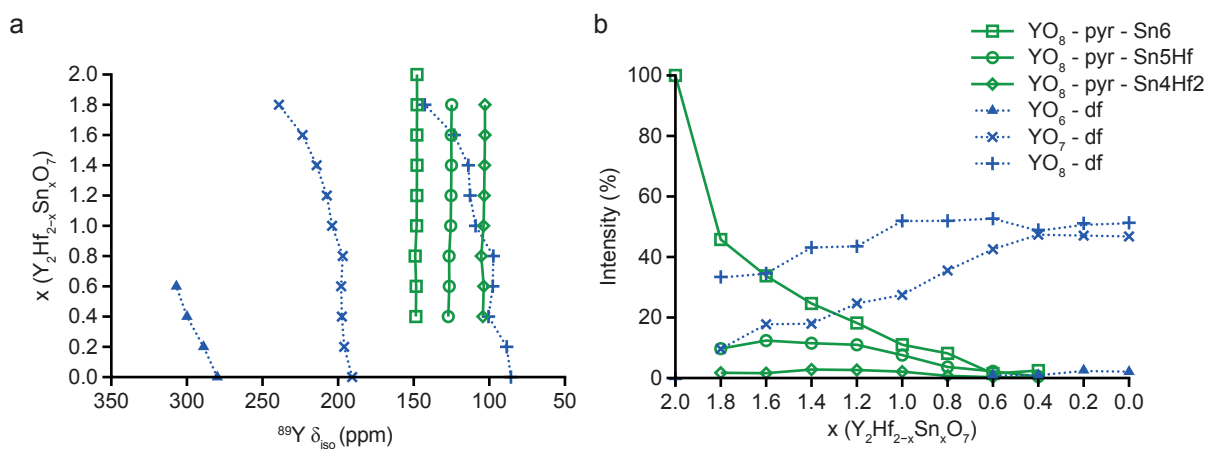
Figure S4.2. Plot showing the variation of (a) chemical shifts and (b) integrated intensities of resonances in the ^{89}Y MAS NMR spectra of $Y_2Hf_{2-x}Sn_xO_7$ with nominal composition. Resonances attributed to the pyrochlore and defect fluorite phases are denoted pyr and df, respectively. For the pyrochlore phase, the B site NNN arrangement for each environment is also shown.

S5. Further information on ¹¹⁹Sn MAS NMR spectra

Figure S5.1 shows the result of the analytical fitting of ¹¹⁹Sn MAS NMR spectra of $Y_2Hf_{0.2}Sn_{1.8}O_7$.
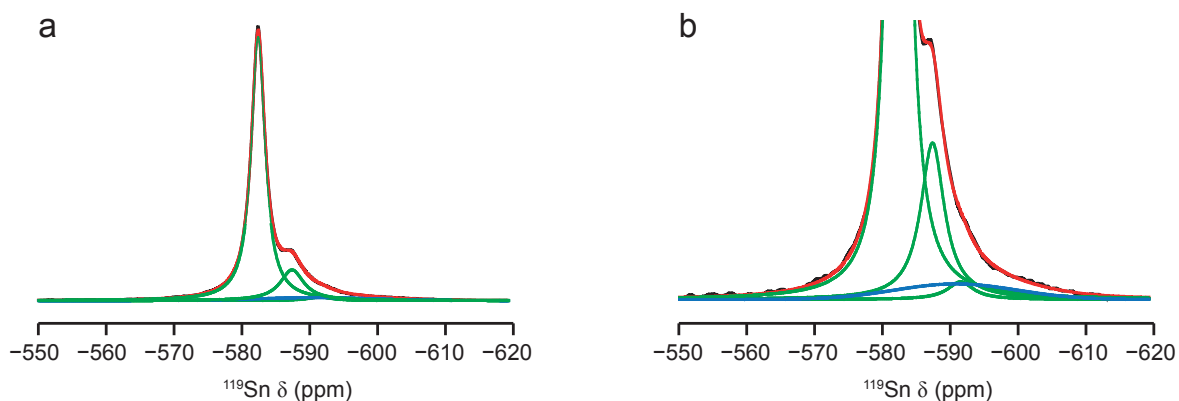
Figure S5.1. (a) Analytical fit and (b) corresponding (vertical) expansion of the ¹¹⁹Sn MAS NMR spectrum of $Y_2Hf_{0.2}Sn_{1.8}O_7$. The green, blue and red lines denote the analytical fit for the pyrochlore phase, defect fluorite phase and all resonances, respectively.

From a fitting of each of the ¹¹⁹Sn MAS NMR spectra of $Y_2Hf_{2-x}Sn_xO_7$ in Figure 5 of the main text, the chemical shifts of the individual components, and their relative intensities can be extracted. These are given in Table 2 (main text) and shown in Figure S5.2 as a function of the composition of the starting materials.
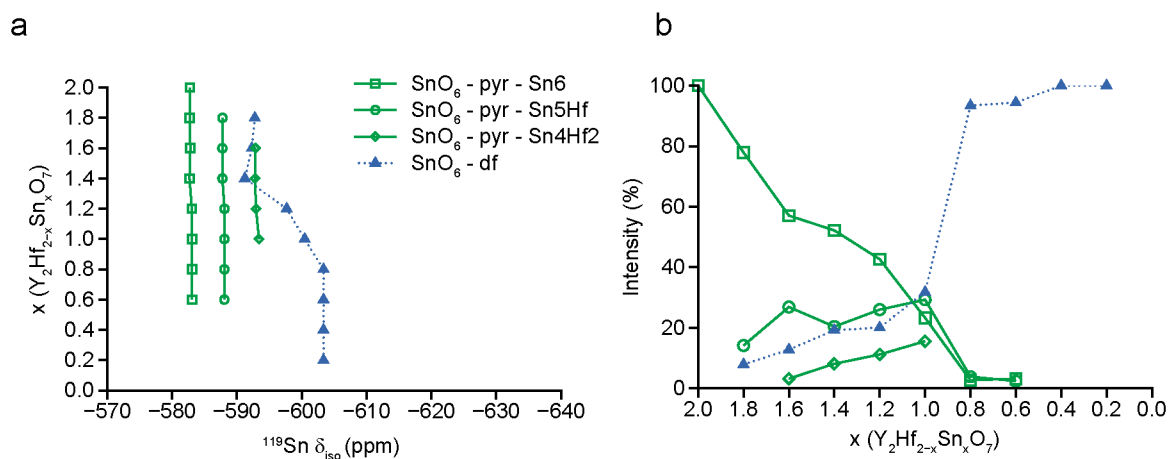
Figure S5.2. Plot showing the variation of (a) chemical shifts and (b) integrated intensities of resonances in the ^{119}Sn MAS NMR spectra of $Y_2Hf_{2-x}Sn_xO_7$ with nominal composition. Resonances attributed to the pyrochlore and defect fluorite phases are denoted pyr and df, respectively. For the pyrochlore phase, the B site NNN arrangement for each environment is also shown.

All of the resonances in the ^{119}Sn NMR spectra in Figure 5 have chemical shifts commonly associated with six-coordinate Sn species, suggesting not only that Sn is confined to the B site in the pyrochlore phase, but that it also adopts six-fold coordination in the disordered defect fluorite phase, *i.e.*, that the vacancies are preferentially associated with Sn over Y or Hf. Figure S5.3 confirms that no signal is seen at shifts corresponding to higher (*i.e.*, seven- and eight-coordinate) Sn species in the ^{119}Sn MAS NMR spectrum of $Y_2Hf_{1.8}Sn_{0.2}O_7$ acquired using a wider spectral width. Here calculated ^{119}Sn δ_{iso} for pyrochlore models of $Y_2Sn_2O_7$ against where oxygen atoms have been moved from 8a to vacant 8b sites thereby changing the Sn coordination number are also shown (as in Figure 6b of the main text).
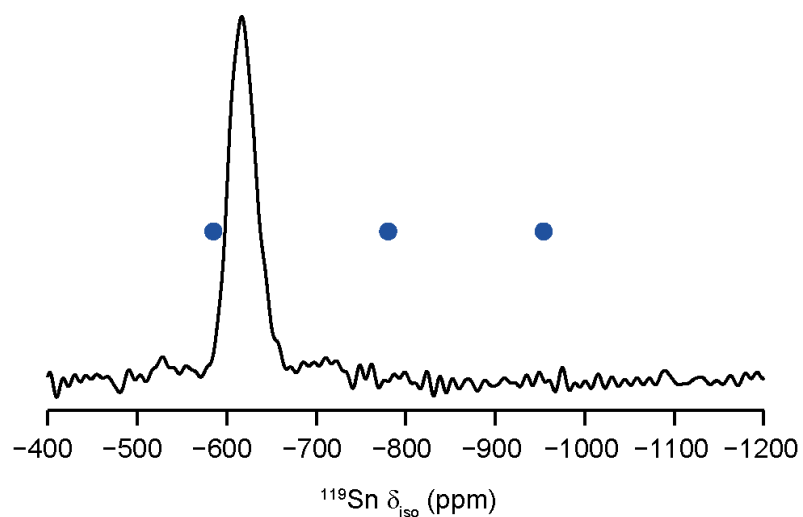
Figure S5.3. ^{119}Sn (9.4 T, 14 kHz) MAS NMR spectrum of $Y_2Hf_{1.8}Sn_{0.2}O_7$, acquired using a spin echo sequence. The blue dots represent calculated ^{119}Sn δ_{iso} for pyrochlore models with six-, seven- and eight-coordinated Sn, as in Figure 6b of the main text.

S6. Further information on ^{17}O MAS NMR spectra

Figure S6.1 shows ^{17}O MAS NMR spectra of a 1 : 1 molar physical mixture of $Y_2Sn_2O_7$ and $Y_2Hf_2O_7$, enriched at two different temperatures. The spectra have been normalised to the intensity of the defect fluorite peak at ~310 ppm. It is clear that at lower temperature the relative level of enrichment of the two phases is different, with preferential enrichment of the defect fluorite ($Y_2Hf_2O_7$) phase. At the higher temperature, the relative intensities of the signals from the pyrochlore and defect fluorite signals are 0.65 : 1.35, not the 1 : 1 that might be expected. As discussed in Ref. S9, there are no differences in nutation of the different signals at the short flip angles used. However, when spectra were acquired with a much longer recycle interval (1500 s), an increase in the intensity of the pyrochlore signals (of 3.35 and 2.2, for O1 and O2, respectively) was observed. For signals with very low C_Q (*i.e.*, O1 in the pyrochlore phase and all signals in the defect fluorite phase), it is also necessary to take into account the contribution of the satellite transitions (ST) to the spectral intensities (see Ref. S9 for further information). Once these corrections (factors of 3.89 for pyrochlore O1 and 1.08 for defect fluorite signals), the relative intensities of the signals from the two phases are 1 : 1, as expected. This demonstrates that uniform relative enrichment of both phases is obtained with enrichment at 900 °C for 12 h.
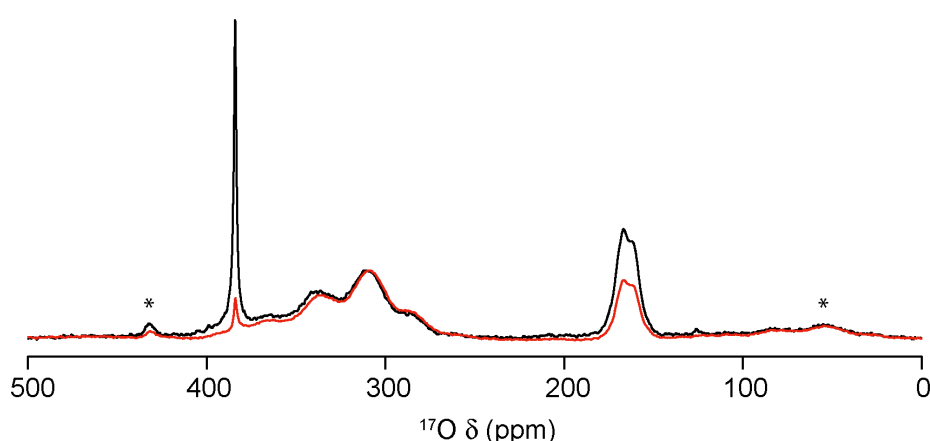
Figure S6.1. ^{17}O (14.1 T, 21 kHz) MAS NMR spectrum of a molar 1 : 1 physical mixture of $Y_2Sn_2O_7$ and $Y_2Hf_2O_7$ enriched at 600 °C (red) and 900 °C (black) for 12 h. The spectra were acquired using a recycle interval of 5 s. Spinning sidebands are marked with *.

Figure S6.3 shows expansions of the ^{17}O (MAS NMR spectra of $Y_2Hf_{2-x}Sn_xO_7$ with x = 1.8, 1.6 and 1.2, confirming the presence of resonances from a defect fluorite phase even at low Hf compositions.
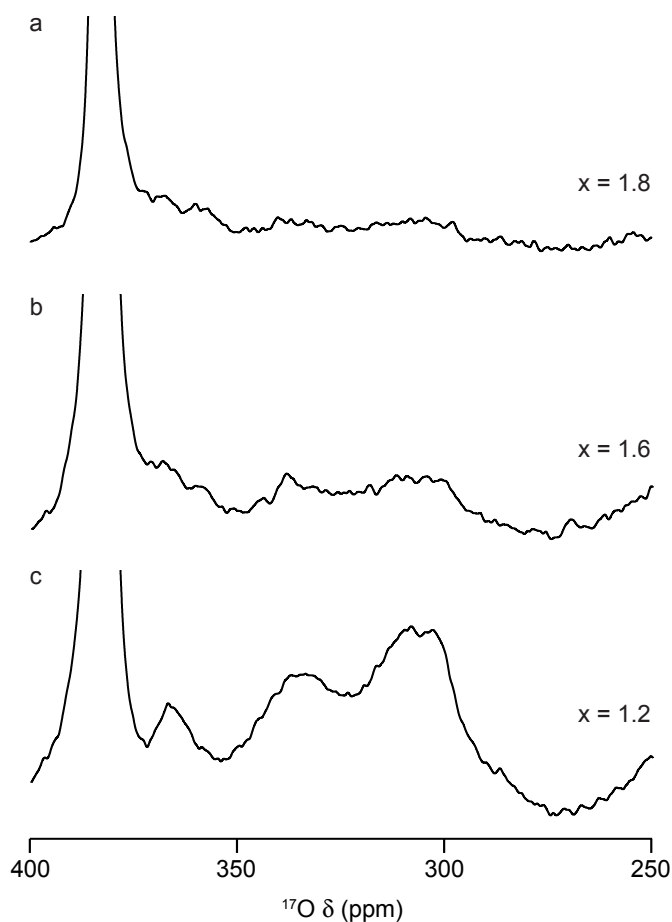
Figure S6.2. Expansions of ^{17}O (14.1 T, 21 kHz) MAS NMR spectra of $Y_2Hf_{2-x}Sn_xO_7$, enriched at 900 °C for 12 h, with x = (a) 1.8, (b) 1.6 and (c) 1.2.

Figure S6.3 shows a ^{17}O MQMAS NMR spectrum of $Y_2Sn_{0.6}Hf_{1.4}O_7$ (expanded to show the region corresponding to OX3Sn) enriched 900 °C for 12 h. The spectrum was acquired using a z-filtered pulse sequence but is shown after shearing, with the δ_1 axis referenced according to the convention in Ref. S14. From the position of the centre-of-gravity of the lineshape values of $\langle\delta_{iso}\rangle \approx$ ~238 ppm and $\langle P_Q\rangle \approx$ ~2.6 MHz can be extracted, demonstrating the broadening observed in the MAS spectrum arises primarily from a distribution of chemical shifts.
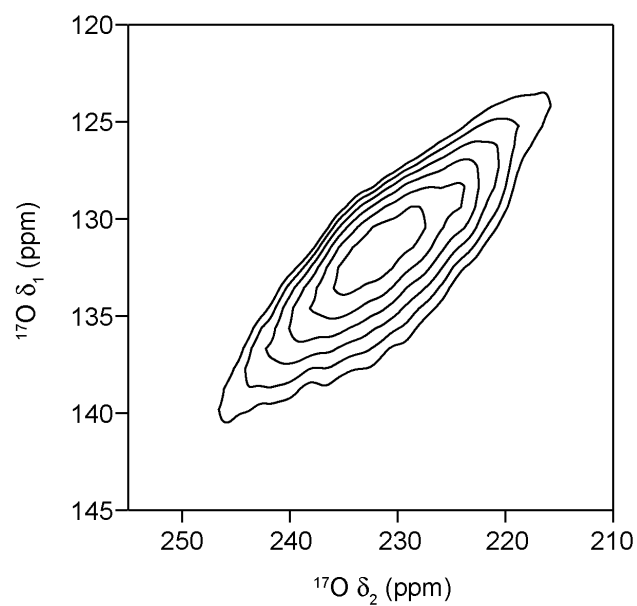
Figure S6.3. ^{17}O (14.1 T, 21 kHz) MQMAS NMR spectrum of $Y_2Sn_{0.6}Hf_{1.4}O_7$ (expanded to show the region corresponding to OX3Sn) enriched 900 °C for 12 h.

S7. Comparison of average coordination numbers in defect fluorite phases

Figure S7.1 compares the variation in average coordination number of Y, Sn and Hf/Zr in $Y_2(Hf,Sn)_2O_7$ and $Y_2(Zr,Sn)_2O_7$ disordered defect fluorite phases as a function of composition. Values for $Y_2(Zr,Sn)_2O_7$ have been taken from Ref. S15.
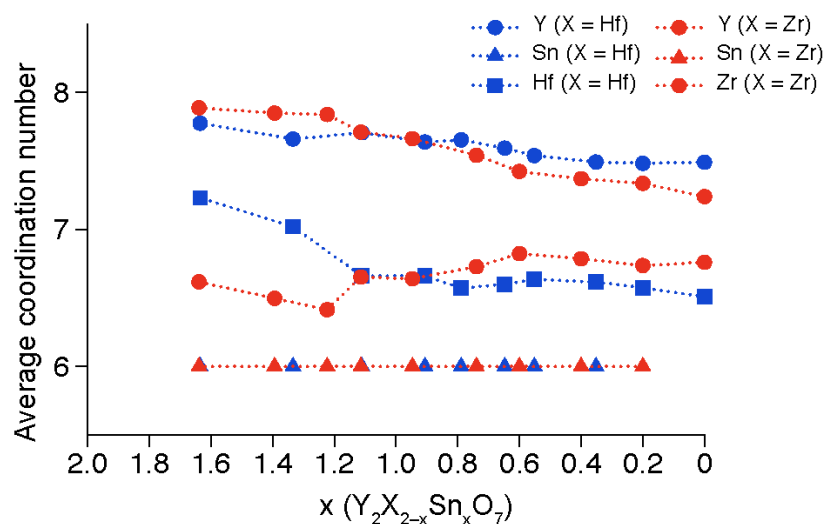
Figure S7.1. Plot showing the variation in average coordination number of Y, Sn and Hf/Zr in disordered defect fluorite $Y_2X_{2-x}Sn_xO_7$ (where X = H or Zr) as a function of the actual (not nominal) composition.

S8. References

S1. Pickard, C. J.; Mauri, F. All-Electron Magnetic Response with Pseudopotentials: NMR Chemical Shifts. *Phys. Rev. B: Condens. Matter Mater. Phys*. **2001**, *63*, 245101.

S2. Clark, S. J.; Segall, M. D.; Pickard, C. J.; Hasnip, P. J.; Probert, M. J.; Refson, K.; Payne, M. C. First-Principles Methods using CASTEP. *Z. Kristallogr. - Cryst. Mater*. **2005**, *220*, 567-570.

S3. Perdew, J. P.; Burke, K.; Ernzerhof, M. Generalized Gradient Approximation Made Simple. *Phys. Rev. Lett*. **1996**, *77*, 1865-1868.

S4. Vanderbilt, D. Soft Self-Consistent Pseudopotentials in a Generalized Eigenvalue Formalism. *Phys. Rev. B: Condens. Matter Mater. Phys*. **1990**, *41*, 7892-7895.

S5. Yates, J. R.; Pickard, C. J.; Payne, M. C.; Mauri, F. Relativistic Nuclear Magnetic Resonance Chemical Shifts of Heavy Nuclei with Pseudopotentials and the Zeroth-Order Regular Approximation. *J. Chem. Phys*. **2003**, *118*, 5746-5743.

S6. Monkhorst, H. J.; Pack, J. D. Special Points for Brillouin-Zone Integrations. *Phys. Rev. B* **1976**, *13*, 5188-5192.

38. Pyykko, P., Year-2017 Nuclear Quadrupole Moments. *Mol. Phys*. **2018,** *116*, 1328-1338.

S7. Moran, R. F. Investigating the use of First-Principles Calculations for NMR Studies in the Solid State. PhD Thesis, University of St Andrews, **2019**.

S8. Grey, C. P.; Dobson, C. M.; Cheetham, A. K.; Jakeman, R. J. B. Studies of Rare-Earth Stannates by ^{119}Sn MAS NMR. The Use of Paramagnetic Shift Probes in the Solid State. *J. Am. Chem. Soc*. **1989**, *111*, 505-511.

S9. Fernandes, A.; Moran, R. F.; Sneddon, S.; Dawson, D. M.; McKay, D.; Bignami, G. P. M.; Blanc, F.; Whittle, K. R.; Ashbrook S. E. ^{17}O Solid-State NMR Spectroscopy of $A_2B_2O_7$ Oxides: Quantitative Isotopic Enrichment and Spectral Acquisition? *RSC Adv*. **2018**, *8*, 7089-7101.

S10. Orr, R. M.; Duer, M. J.; Ashbrook, S. E. Correlating Fast and Slow Chemical Shift Spinning Sideband Patterns in Solid-State NMR. *J. Magn. Reson*. **2005**, *174*, 301-309.

S11. Orr, R. M.; Duer, M. J. Applications of the CSA-Amplified PASS Experiment. *Solid State Nucl. Magn. Reson*. **2006**, *30*, 1-8.

S12. Levitt, M. H.; Madhu, P. K.; Hughes, C. E. Cogwheel Phase Cycling. *J. Magn. Reson.* **2002**, *155*, 300-306.

S13. Bak, M.; Rasmussen, J.; Nielsen, N. SIMPSON: a General Simulation Program for Solid-State NMR Spectroscopy. *J. Magn. Reson*. **2000**, *147*, 296-330.

S14. Pike, K. J.; Malde, R. P.; Ashbrook, S. E.; McManus, J.; Wimperis, S. Multiple-Quantum MAS NMR of Quadrupolar Nuclei. Do Five-, Seven- and Nine-Quantum Experiments Yield Higher Resolution than the Three-Quantum Experiment? *Solid State Nucl. Magn. Reson*. **2000**, *16*, 203-215.

S15. Ashbrook, S. E.; Mitchell, M. R.; Sneddon, S.; Moran, R. F.; de los Reyes, M.; Lumpkin G. R.; Whittle, K. R. New Insights into Phase Distribution, Phase Composition and Disorder in $Y_2(Zr,Sn)_2O_7$ Ceramics from NMR Spectroscopy. *Phys. Chem. Chem. Phys.* **2015**, *17*, 9049-9059.